

1 **A reappraisal of igneous emplacement mechanisms: evidence from deformation**  
2 **structures, Trachyte Mesa intrusion, Henry Mountains, Utah**

3 \*Penelope I. R. Wilson<sup>1</sup>, Kenneth J. W. McCaffrey<sup>2</sup>, Robert W. Wilson<sup>3</sup>, and Ian Jarvis<sup>1</sup>

4

5 <sup>1</sup> School of Geography, Geology and the Environment, Kingston University London, Kingston  
6 upon Thames KT1 2EE, UK

7 <sup>2</sup> Department of Earth Sciences, Durham University, Science Labs, Durham DH1 3LE, UK

8 <sup>3</sup> BP Exploration Operating Company Ltd., Chertsey Road, Sunbury on Thames TW16 7LN, UK

9

10 Corresponding author contact details–

11 Email address: [penelope.small@gmail.com](mailto:penelope.small@gmail.com) (or [p.wilson@kingston.ac.uk](mailto:p.wilson@kingston.ac.uk))

12 Postal address: 32 Auckland Road, Kingston-upon-Thames KT1 3BG, UK

13 Telephone number: +44 (0)7809 826049

14

15 Co-author email addresses:

16 [k.j.w.mccaffrey@durham.ac.uk](mailto:k.j.w.mccaffrey@durham.ac.uk)

17 [woody.wilson@uk.bp.com](mailto:woody.wilson@uk.bp.com)

18 [i.jarvis@kingston.ac.uk](mailto:i.jarvis@kingston.ac.uk)

19

20 **Abstract**

21 Deformation structures in host rocks to high level igneous intrusions potentially record how  
22 magma is emplaced and accommodated within the shallow crust. Trachyte Mesa, a small  
23 intrusion in the Henry Mountains, Utah, is comprised of a series of stacked sheets. New  
24 structural analysis of the kinematic, spatial and temporal distribution of deformation  
25 structures in the host rocks to the intrusion has enabled the recognition of three distinct  
26 phases, interpreted to represent pre- (Phase 1), syn- (2A and 2B), and late-stage- (3)  
27 emplacement deformation. In this paper we present a new 5 stage model for the  
28 emplacement of Trachyte Mesa, following a two-stage growth mechanism for individual  
29 sheets, with radial growth of a thin sheet followed by vertical inflation. Syn-emplacement  
30 structures are localised to the intrusion lateral margins: prolific deformation bands  
31 widespread over the margin; and dip-slip faults restricted to the tips of individual sheets due  
32 to strain localisation during vertical inflation. Magma preferentially exploited these faults,  
33 initiating sill climbing. The order in which sheets are stacked impacts on the intrusion  
34 geometry and associated deformation. Our results offer new insights into the incremental  
35 intrusion geometries of high level magmatic bodies and the potential impact of their  
36 emplacement on surrounding sedimentary rocks.

37

38 **Keywords:**

39 Deformation Bands; Faults; Intrusion; Sill; Laccolith; Emplacement Mechanism

40

41 **1. Introduction**

42 High-level sill and laccolith complexes are an important part of sub-volcanic plumbing  
43 systems in which magma is emplaced as a series of sub-horizontal tabular sheet-like  
44 intrusions (Cruden and McCaffrey, 2001). Most studies of magmatic intrusions have  
45 concentrated on their geometry and internal architecture (Du Toit, 1920; Thompson, 2004;  
46 Thompson and Hutton, 2004; Thompson and Schofield, 2008; Schofield et al., 2012); whilst  
47 few have paid particular attention to emplacement-related deformation structures in the  
48 host rock. Yet these potentially record how magma is accommodated within the crust,  
49 shedding light on the so-called 'space problem' (Hutton, 1996, 1997; Tikoff et al., 2013;  
50 Wilson et al., In Prep.).

51

52 Mounting evidence suggests that many high-level crustal intrusions (both plutonic and  
53 small-scale satellite intrusions) are emplaced and grow through incremental addition of  
54 small volumes of magma (e.g. Pitcher, 1970; Mahan et al., 2003; Glazner et al., 2004;  
55 Morgan et al., 2008). Furthermore, recent studies have shown that tabular intrusions are  
56 often emplaced by the amalgamation of magma fingers, sheets and lobes (Pollard et al.,  
57 1975; Horsman et al., 2005; Stevenson et al., 2007a; Morgan et al., 2005, 2008; Schofield et  
58 al., 2010). This internal architecture has been resolved by a number of different methods,  
59 including magnetic and macroscopic fabric studies (de Saint Blanquat and Tikoff, 1997;  
60 Horsman et al., 2005; Stevenson et al., 2007b), field mapping of internal contacts (Morgan  
61 et al., 2008; Magee et al., 2012) and geochronology (Coleman et al., 2004; Westerman et al.,  
62 2004). A few authors (e.g. Johnson and Pollard, 1973; Jackson and Pollard, 1990; Morgan et

63 al., 2008) have studied how the host rocks deform as intrusions grow, crystallize and  
64 ultimately cool to ambient temperatures.

65

66 Hunt (1953) outlined three general emplacement models for high level intrusions: (1) radial  
67 growth only, with magma emplaced at a constant thickness and country rocks displaced  
68 both vertically and laterally (i.e. a “bulldozing” mechanism; Model B of Hunt, 1953, fig. 70, p.  
69 142); (2) two-stage growth, comprising radial growth of a thin sheet followed by dominantly  
70 vertical growth and associated vertical uplift of the overriding host rocks (i.e. a “two-stage  
71 growth” mechanism; Model A of Hunt, 1953); and (3) simultaneous vertical and horizontal  
72 growth (Model C of Hunt, 1953). Various hybrid models have since been described following  
73 increased understanding of the nature of intrusive geometries, and evidence that bodies are  
74 commonly comprised by a number of smaller sheets and finger-like-lobes (e.g. Christmas-  
75 tree or Cedar-tree laccoliths; Corry, 1988). Deformation structures associated with  
76 emplacement are strongly linked to the mechanism of emplacement (Corry, 1988, figs 14–  
77 16, pp. 16–17); however, few studies have specifically targeted these structures in detail.

78

79 In this paper, we present a new structural analysis of the kinematic, spatial and temporal  
80 distribution of deformation structures in the host rocks to the Trachyte Mesa intrusion, a  
81 small satellite intrusion to the Mount Hillers intrusive complex, Henry Mountains, Utah,  
82 U.S.A. (Fig. 1). By integrating the host rock structures with the sequential intrusion history  
83 and building on previous studies (e.g. Gilbert, 1877; Johnson and Pollard, 1973; Morgan et  
84 al., 2008; Wetmore et al., 2009), we have created a new improved model for the  
85 emplacement of Trachyte Mesa. The results offer new insights into the incremental



86 intrusion geometries of high level magmatic bodies and the potential impact of their  
87 emplacement on surrounding sedimentary rocks.

88

## 89 **2. Geological Setting**

### 90 *2.1. Henry Mountains*

91 The Henry Mountains, located in SE Utah on the Colorado Plateau (Fig. 1a), are a type  
92 locality for the study of igneous intrusions and their emplacement. It was here that Gilbert  
93 (1877) famously first described and named laccoliths (coining the term “laccolite”; Gilbert,  
94 1896) in terms of their modes of formation rather than their geometry. Accordingly,  
95 laccoliths are formed as a result of magma that “insinuated itself between two strata, and  
96 opened for itself a chamber by lifting all the superior beds” (Gilbert, 1877). Since the  
97 ground-breaking work of Gilbert, undertaken during an expedition to the Henry Mountains  
98 as part of the Powell Survey along the Green and Colorado Rivers, a number of studies have  
99 been carried out in the range (Hunt, 1953; Johnson and Pollard, 1973; Jackson and Pollard,  
100 1988; Nelson and Davidson, 1993; Habert and de Saint Blanquat, 2004; Horsman et al.,  
101 2005; Morgan et al., 2005; de Saint-Blanquat et al., 2006; Wetmore et al., 2009; Wilson and  
102 McCaffrey, 2013).

103

104 The Henry Mountains consist of five principal peaks, each signifying a distinct intrusive  
105 centre. From north to south these are: Mt Ellen; Mt Pennell; Mt Hillers; Mt Holmes; and Mt  
106 Ellsworth (Fig. 1a). The intrusions are mid-Tertiary in age (Oligocene, 31.2 to 23.3 Ma K-Ar  
107 ages; Nelson et al., 1992), emplaced within a ~2.7 km thick section of Palaeozoic  
108 sedimentary rocks overlying Precambrian crystalline basement (Jackson and Pollard, 1988).

109 Most of the intrusions have a consistent dioritic composition (58–63% SiO<sub>2</sub>; Hunt, 1953;  
110 Engel, 1959; Nelson et al., 1992). The diorite has a porphyritic texture, with dominant  
111 feldspar (An<sub>20</sub> to An<sub>60</sub>; 20–40%) and hornblende (5–15%) phenocrysts (i.e. plagioclase-  
112 hornblende porphyry), the textural characteristics varying significantly from one intrusion to  
113 another (Hunt, 1953; Nelson et al., 1992).

114

115 The intrusions post-date minor Laramide orogenic activity (Late Cretaceous to Early Tertiary  
116 in age; Davis, 1978, 1999) on the Colorado Plateau. Although Laramide structures, such as  
117 the N–S trending Waterpocket Fold (part of the greater Circle Cliffs uplift; Davis, 1978;  
118 Jackson and Pollard, 1988; Bump and Davis, 2003) can be found locally, the strata into which  
119 the Henry Mountains intrusions are emplaced are nearly flat lying (gently dipping ~2° to the  
120 east; Jackson and Pollard, 1988). Lack of significant pre- and post-emplacement tectonism  
121 aids the identification of emplacement-related deformation structures and has preserved  
122 the original magmatic and solid-state fabrics within the intrusive bodies.

123

## 124 2.2. *Trachyte Mesa*

125 The Trachyte Mesa intrusion (also known as the “Howell laccolith” in the work of Gilbert;  
126 Hunt, 1988) is the most distal satellite intrusion of the Mount Hillers intrusive complex,  
127 located some 12 km to the NE of the central complex (11 in Fig. 1b). The intrusion has an  
128 elongate (~2.2 km long and 0.7 km wide) laccolithic geometry, trending NE–SW (Fig. 2).  
129 Thicknesses observed in cliff exposures range from 5 m to 50 m (Morgan et al., 2008), with  
130 an average thickness, estimated from magnetic and resistivity studies, of ~15 m (Wetmore  
131 et al., 2009). Various models have been suggested for the geometry and internal

132 architecture of the intrusion, ranging from a single domal “laccolitic” body (Gilbert, 1887;  
133 Hunt, 1953; Wetmore et al., 2009), to a series of stacked intrusive sheets and lobes  
134 (Johnson and Pollard, 1973; Morgan et al., 2005, 2008; Fig. 2d, e). In the exposures  
135 described by Morgan et al. (2008), a complex stacking history may be interpreted, with  
136 earlier sub-horizontally stacked intrusive sheets at the top of the sequence being flexed and  
137 arched by the emplacement of later sub-horizontally stacked tongue-like sheets beneath  
138 (Fig. 2d, e). These were evaluated further in the present study. Favouring the stacked  
139 intrusive sheet model, Morgan et al. (2008) questioned the use of the term “laccolith” for  
140 Trachyte Mesa, suggesting that it has features that represent a hybrid between a sill and a  
141 laccolith; however, from a geometric perspective, they agreed that laccolith is a reasonable  
142 term (i.e. upward doming at the roof of the intrusion).

143

144 The present-day local geomorphology closely resembles that of the original intrusion (Fig.  
145 2a–b). This assertion is supported by the presence of multiple intrusion-host-rock contacts  
146 on the top and NW margins of the intrusion, although the SE margin is less well constrained  
147 (Morgan et al., 2008). The mesa has a relatively flat top with steeper NW and SE lateral  
148 margins. Where exposed, the base of the overall intrusion appears to be relatively  
149 concordant with the underlying sandstone, dipping  $<10^\circ$  to the NW. Wetmore et al. (2009)  
150 concluded that the trend of the intrusion was controlled by a series of NE–SW trending pre-  
151 existing (Laramide?) folds, and they suggested that the axis of the intrusion may lie within a  
152 syncline. Regionally there is support for the NE–SW folding proposed by Wetmore et al.  
153 (2009); however, the local bedding and base intrusion contact exposures do not support the  
154 model for a tight syncline along the axis of the Trachyte Mesa intrusion. We note that this  
155 synclinal geometry was interpreted from magnetic data and is, therefore, potentially a non-

156 unique solution to the geophysical data acquired. The area analysed by Wetmore et al.  
157 (2009) lies to the SW of the exposed intrusion geometries, and an alternative interpretation  
158 for this deeper synclinal geometry at the base of the intrusion is that it represents a deeper  
159 feeder system to the intrusion, which propagated from the SW. The more flat lying, NW  
160 dipping monoclinical geometry of Morgan et al. (2008) is favoured here.

161

162 In contrast to the relatively flat lying stratigraphy below the intrusion, the host-rock units  
163 above show significant distortion and deformation (Johnson and Pollard, 1973; Morgan et  
164 al. 2008). At the NW margin of the intrusion, a clear monoclinical bending of the overlying  
165 beds is apparent (Fig. 2e), which is interpreted to be the result of vertical and lateral growth  
166 of the intrusion (Gilbert, 1887; Hunt, 1953; Johnson and Pollard, 1973; Morgan et al., 2008).  
167 As discussed above, the intrusion is generally concordant with the Entrada Sandstone  
168 Formation, within which it is emplaced (Johnson and Pollard, 1973; Morgan et al., 2008;  
169 Wetmore et al., 2009). The Entrada Sandstone Formation (part of the San Rafael Group) is  
170 Late Jurassic in age and is composed of a mixture of white cross-bedded sandstones,  
171 reddish-brown silty sandstones, siltstones, and shale beds (Aydin, 1978). The Entrada  
172 Sandstone, being highly porous, is the ideal lithology for the formation of deformation  
173 bands and, as a result (along with the Lower Jurassic Navajo Sandstone, also found on the  
174 Colorado Plateau and stratigraphically below the Entrada; Jackson and Pollard, 1988), has  
175 been the focus of several studies on such structures (Aydin, 1978; Aydin and Johnson, 1978,  
176 1983; Shipton and Cowie, 2001; Fossen et al., 2007).

177

178 Our field study focused on the southern end of the NW lateral intrusion margin (outlined in  
179 Fig. 2) as this area offers the best exposure of the intrusion and its contact with overlying  
180 host rocks (Fig. 2b, e). Detailed kinematic and geometrical studies were carried out at  
181 numerous outcrops, regularly spaced along two approximately N–S structural transects  
182 across the NW margin (TMTE and TMTW in Fig. 2c), and at additional outcrops close to  
183 intrusion contacts (including area TMT3; Fig. 2c). At each structural station, a representative  
184 structural dataset (including: deformation type; geometry; kinematics; phase; character)  
185 was collected (minimum of 30 measurements per station; >50 in areas of high intensity  
186 deformation).

187

### 188 **3. Intrusion Geometry**

189 Figure 3 provides an overview of the intrusion contact relationships on the NW margin  
190 where we carried out our structural transects (TMTE and TMTW). Multiple sill sheets and  
191 sheet terminations can be observed that appear to be stacked to create the greater  
192 intrusive body (Fig. 2d, e). Along transect TMTE (Trachyte Mesa Transect East; Fig. 2c) from  
193 NW to SE a distinct monoclinial geometry can be seen (Fig. 3a), both within the upper sill  
194 sheets and the overriding sandstone beds. Bedding in this monocline goes from sub-  
195 horizontal on the top of the mesa to dips of up to  $\sim 40^\circ$  on the lateral margin (Figs 2e, 3),  
196 back to sub-horizontal at the NW end. Lower sub-horizontal sill sheets are also apparent,  
197 sandwiched between these upper and lower sheets in a zone of highly deformed sandstone  
198 with little to no depositional characteristics preserved (Fig. 3a). A common feature of many  
199 of the sill sheets is their “bulbous” to sub-vertical sheet terminations, which generally trend  
200 parallel to the overall intrusion margin (c. NE–SW; Fig. 3). Morgan et al. (2008) provided a  
201 comprehensive review of the stacked sill sheet geometries in this area.

202

203 The monoclinical geometry appears to be discontinuous along the margin. Along transect  
204 TMTW (Trachyte Mesa Transect West; Figs 2c, 3b), ~200 m SE of the outcrops described  
205 above, multiple sub-horizontal sheets can be seen stacked one on top of the other, with  
206 sheet terminations stepping back onto the top of the overall intrusive body. Furthermore,  
207 the morphology of the overriding sandstone appears more complex and step-like, mimicking  
208 the underlying sill sheet geometry (Fig. 3b). In this same area, upward-inclined sheet  
209 geometries can also be seen, which possibly reflect sill climbing during emplacement. In  
210 area TMT3 (Fig. 2c), intrusion geometries are less well exposed, however, the overlying  
211 sandstone units resemble the more step-like / terrace geometry seen along transect TMTW.

212

## 213 4. Deformation Structures

### 214 4.1. Structural types and geometry

215 As noted above, locally, bedding has been deformed to form a monoclinical fold across the  
216 NW lateral margin of the intrusion, with dips ranging from sub-horizontal to ~40° to the NW  
217 on the steep limb (Figs 2, 4a). Deformation structures observed within the Entrada  
218 Sandstone host rock include: prolific deformation bands; dip-slip faults; and opening (Mode  
219 1) joints (Figs 4b–d, 5). Most of the deformation bands are porosity reducing and cataclastic  
220 in character, showing small (mm- to cm-scale) offsets. There is a wide variation in  
221 deformation band orientation, with a dominant NE–SW trend, paralleling that of the  
222 intrusion (Figs 2a, 4b). Locally, small populations of dip-slip faults are observed, that trend  
223 parallel to the intrusion margin (NE–SW and ESE–WNW locally; Fig. 4c). A more widely  
224 distributed system of opening mode joints, striking both parallel and perpendicular to the  
225 intrusion margin, is also observed (Fig. 4d). These joints commonly show evidence for fluid

226 migration, with fine white carbonate precipitates and/or well-developed calcite crystals (Fig.  
227 5g) on joint surfaces. Furthermore, apparent fluid-escape structures can be seen exploiting  
228 joints on the top surface of the intrusion (Fig. 5h).

229

230 Various shear zones are observed within the intrusion and on the top surface (a number of  
231 which were described by Morgan et al., 2008). Within the host-rock these are restricted to  
232 the reddish-brown silty sandstone and shale unit that is commonly observed immediately  
233 above the intrusion, and is not apparent in the more massive red sandstone units above  
234 (Fig. 5b). In the upper few centimetres of individual intrusive sheets, and at the interface  
235 between the intrusive sheets, a highly foliated (sub-horizontal foliation) zone occurs with  
236 significant stretched plagioclase phenocrysts (see fig. 3a in Morgan et al., 2008). The shear  
237 sense on structures on the top surface of the intrusion indicate a top-to-the-SE movement  
238 (i.e. reflecting the outward, NW-oriented, horizontal motion of the underlying intrusive  
239 sheet; Fig. 5b).

240

#### 241 *4.2. Structural Phases*

242 Deformation structures observed within the host rocks to the intrusion may be categorised  
243 into three distinct phases, according to: structural type; deformation character; geometry;  
244 kinematics; spacing / intensity; and cross-cutting relationships observed in the field (Figs 4e–  
245 h, 5).

246

247 Phase 1 consists of a set of deformation bands and extensional faults, trending oblique  
248 (ENE-WSW) to the NE-SW trend of the intrusion (Figs 4e, 5a), and were found over a wide

249 area away from the intrusion. Phase 1 deformation bands are discrete and are often  
250 identified by offsets on bedding and cross-beds. Where significant offsets (cm- to m-scale)  
251 are seen, the sense of shear is largely extensional. Phase 1 structures display a low- to  
252 moderate-intensity, with spacing between 50 cm to 100 cm. However, high intensity (cm-  
253 scale spacing) ladder structures / deformation corridors also occur. Phase 1 structures are  
254 interpreted as being related to regional structure that predated the intense deformation  
255 that was associated with emplacement of the intrusion because they occur at distances  
256 away from the intrusion

257

258 Phase 2 comprises a second set of deformation bands and faults (Figs 4f–g, 5b–d, 6) that  
259 overprint the earlier Phase 1 structures. Both the deformation bands and the faults trend  
260 NE–SW, parallel to the NW lateral margin and overall trend of the intrusion. In contrast to  
261 Phase 1 deformation bands, Phase 2 structures are much more readily visible in exposures,  
262 often occurring as resistant ridges (ribbed character) standing proud of the host Entrada  
263 Sandstone (Fig. 5c). Microstructural analysis of these Phase 2 deformation bands shows  
264 them to be largely created as a result of cataclasis and compaction, with significant (almost  
265 100%) porosity reduction along the deformation bands. The intensity (fracture density) of  
266 Phase 2 deformation bands is significantly higher than that of Phase 1, with fracture spacing  
267 in the order of 0.5 cm to 5 cm, although intensity decreases rapidly as you move off the  
268 intrusion margin.

269



270 Phase 2 deformation bands form conjugate sets with extensional offsets (Fig. 6a, b). Phase 2  
271 faults are dip-slip in character, showing both normal and reverse movements (Fig. 4c, g), but  
272 with a common down to the NW offset (Fig. 6c-e). Unlike Phase 1 extensional faults, these  
273 often show a distinct principal slip surface (PSS; Fig. 6e), and slickenlines are commonly  
274 observed (Figs 4g, 5d). Phase 2 structures can be sub-divided further according to their  
275 cross-cutting relationships. Deformation bands (Phase 2A) are consistently cross-cut by the  
276 dip-slip faults (Phase 2B), as well as steeply dipping ladder zones (Fig. 6 c–e).

277

278 Phase 3 comprises a system of tensile joints, often infilled with calcite crystals, which  
279 overprint all other deformation structures (Figs 4h, 5e–h). The system of joints consists of  
280 two sets: a NW–SE trending set, perpendicular to the intrusion margin (Fig. 5e); and a NE–  
281 SW trending set, sub-parallel to the intrusion margin (Fig. 5f). No clear cross-cutting  
282 relationship is apparent between these two joint sets.

283

## 284 **5. Spatial distribution of structures**

285 As part of the fieldwork program, all structural data were georeferenced within a  
286 FieldMove™ project (Fig. 2) in order to capture their spatial distribution. FieldMove™ was  
287 chosen due to the ability to easily transfer the data between the various Move™ software  
288 programs in order to build models (3D Move™), create cross-sections of bedding data (2D  
289 Move™), and ultimately carry out kinematic modelling.

290

### 291 **5.1. Structural transect profiles**

292 Distinct structural domains were identified along the two structural transects (TMTW and  
293 TMTE) within the host rock that reflect both temporal and kinematic variations in  
294 deformation. The structural data at individual stations are plotted on two composite cross  
295 sections created in Move (Figs 7, 8). It is clear from these cross sections that Phase 1  
296 deformation structures are only identifiable at more distal structural stations to the  
297 intrusion margin, and are overprinted by Phase 2A, 2B and 3 deformation structures with  
298 increased proximity to the intrusion. Phase 2 structures increase in intensity from just  
299 outboard of the intrusion margin, and onto the top surface of the intrusion. Phase 2A  
300 conjugate deformation bands appear to rotate about a horizontal axis in the vicinity of the  
301 flanking monocline (Figs 6a, 7, 8).

302

303 Bedding along the western section (TMTW) displays a stepped geometry with each step  
304 appearing to be associated with a new intrusive sill sheet (Fig. 7). Deformation structures  
305 vary across these 'stepped' zones, with Phase 2B (faults and steep ladder zones) appearing  
306 localised to sill sheet terminations (Figs 6d, 7). In contrast, bedding geometry appears  
307 simpler in the eastern cross section (TMTE), the monoclinial structure, lacking the 'steps'  
308 observed for TMTW. Accordingly, Phase 2B faults are also rare along the outcrops of  
309 transect TMTE (Fig. 8).

310

### 311 *5.2. Variations with intrusion margin trend*

312 Phase 2B, steep dip-slip (normal and reverse) faults are most commonly observed on the  
313 intrusion margin, associated with the tips / terminations of intrusive sheets (Fig. 6d, e).  
314 Phase 2B faults are largely observed only at structural station outcrops on the structural

315 transect TMTW and additional TMT3 outcrops (Figs 2c, 9). Mapping of these faults along  
316 strike reveal an arcuate trend that appears to match the proposed curved nature of the  
317 'lobe' / promontory of stacked intrusive sheets (Morgan et al., 2008; Wetmore et al., 2010)  
318 emanating from the main intrusion (Fig. 9). There is a distinct lack of Phase 2B faults in the  
319 vicinity of transect TMTE. We believe this may be due to the style of emplacement in this  
320 area.

321

### 322 *5.3. Deformation structures at the intrusion contact*

323 Deformation microstructures within the sheared upper contact of the intrusion show brittle  
324 to brittle-ductile deformation structures (Figs 10, 11). At the tip and frontal edge of the  
325 intrusion contact, sub-vertical fractures and shear bands (with down-to-the-NW kinematics)  
326 may be seen (Fig. 10a, d). Similar to those observed at outcrop, stepped intrusion  
327 geometries are observed at the micro scale, with steps appearing to be associated with sub-  
328 vertical shear-fractures within the host rock (Fig. 10a). These fractures do not appear to  
329 extend into the intrusion and are therefore likely to be linked to the emplacement of the  
330 magma. Furthermore, magma can also be seen exploiting these sub-vertical shear-fractures  
331 (Fig. 10b).

332

333 Further deformation structures can be found on the top surface of the intrusion. Where the  
334 contact between intrusive sheets and the host rock can be observed, three distinct layers  
335 can be defined (Fig. 10): (1) a 5–10 cm thick baked sandstone layer; (2) a <1 cm thick chilled  
336 intrusion margin; and (3) a 1–2 cm zone of aligned (NW–SE) stretched plagioclase  
337 phenocrysts (beneath this zone mineral alignment decreases significantly). Low-angle

338 fracture planes bisect the baked sandstone horizon (Fig. 11a) but do not appear to extend  
339 into the intrusion (detaching at the contact?). These fracture planes trend parallel to the  
340 intrusion margin (NE–SW), and dip shallowly ( $\sim 20^\circ$ ) to the SE (Fig. 11a). Slickenlines are  
341 preserved on the shear planes in the baked sandstone horizon of the intrusion-host rock  
342 contact, showing down-to-the-SE kinematics.

343

344 These structures are interpreted to be Riedel shear (R1) fractures consistent with a top-to-  
345 the-SE shear sense. Microstructural analysis of the stretched feldspar phenocrysts on the  
346 top surface of the intrusive sill sheets (Fig. 11b) indicates significant brittle deformation with  
347 shearing of the phenocrysts along multiple fracture planes (Fig. 11c). Kinematics of these  
348 fracture planes are also consistent with Riedel shear fractures associated with top-to-the-SE  
349 ( $140^\circ$ ) shear (Fig. 11d).

350

## 351 6. Kinematics

352 Kinematic indicators on Phase 2B dip-slip faults are clearly identifiable as offsets on bedding  
353 planes, and steps on slickenlines preserved on the fault surfaces (Figs 4g, 6, 9). The dip-slip  
354 faults have both normal and reverse kinematics, with a predominant down-to-the-NW  
355 movement, consistent with an overall NW–SE extension or flexure across the margin of the  
356 intrusion (Fig. 6c–e). Sense of slip on Phase 2A deformation bands mirrors the kinematics of  
357 the Phase 2B faults (Fig. 6a, b), although they are distributed more widely across the  
358 intrusion margin. Conjugate sets of extensional deformation bands commonly have an  
359 inclined acute bisector axis, consistent with either an original moderately inclined  $\sigma_3$  axis  
360 dipping towards the NW, or alternatively rotation about a broadly horizontal axis post-

361 formation. In either case, the Phase2B fault kinematics are consistent with accommodation  
362 of down-to-the-NW extension and rotation.

363

364 Strain inversion has been carried out following the Minimized Principal Stress Variation  
365 method developed by Reches (1987) using MyFault™ software. This method assumes that  
366 the stress required to cause fault slip obeys a Coulomb yield criterion. It is considered that  
367 this “strain inversion” technique gives a good approximation for the local palaeostress  
368 associated with the intrusion, as the finite slip on faults is relatively small and therefore  
369 minimal rotation is likely to have occurred (i.e. strain is a good proxy for stress in low strain  
370 environments). Figure 9 shows the bulk inversion for all Phase 2B faults (Fig. 9b), as well as  
371 each individual structural station where faults were observed (Fig. 9c). However, it should  
372 be noted that significant populations of dip-slip faults were only observed at a limited  
373 number of locations (TMTW-3, TMT3-3, TMT3-4, Fig. 9). Bulk inversion suggests that the  
374 main stress acting on these faults was extensional (i.e. sub-vertical  $\sigma_1$ ), with NW–SE (margin  
375 perpendicular) oriented extension. Inclination of the stress axes also reflects the flexural  
376 component of this extension ( $\sigma_3 = 338/20$ ;  $\sigma_1 = 160/70$ ), with extension inclined down  
377 towards the NW. Comparisons of the strain inversion at individual structural stations  
378 highlight distinct local variations. Spatial variation is observed in the orientation of dip-slip  
379 faults, and the kinematic inversion of these individual fault populations reveals a change in  
380 the local extensional strain along the intrusion margin (extension varying from NW–SE to  
381 NNE–SSW; Fig. 9c). Local variations appear to reflect changes in the stress field, mimicking  
382 changes in the orientation of the intrusion margin.

383

384 **7. Discussion**

385        *7.1. Deformation phases (pre-, syn-, and late-stage emplacement)*

386        The three distinct deformation phases identified on the north-western margin of the  
387        Trachyte Mesa intrusion may be directly linked to specific stages in an emplacement model  
388        (pre- Phase 1, syn- Phase 2A and 2B, and late-stage- Phase 3 emplacement).

389

390                *7.1.1. Phase 1 – Pre-emplacment deformation*

391        Phase 1 deformation structures are found throughout the Trachyte Mesa area, including  
392        regions that are significantly distal to the intrusion (Figs 7, 8). As Phase 1 structures do not  
393        show any significant spatial or geometric affinity to the Trachyte Mesa intrusion, we suggest  
394        that these are likely to have developed prior to emplacement. This is also supported by the  
395        consistent cross-cutting relationship observed in the field (i.e. Phase 2 overprinting Phase 1).

396

397        Phase 1 deformation structures could be attributed to one or more of a number of late  
398        Cretaceous to early Tertiary Laramide uplift deformation events (including the San Rafael  
399        Swell, Uncompahgre, Monument, Kaibab, Circle Cliffs, and Miners Mountain uplifts) which  
400        resulted in the formation of a series of asymmetrical anticlines (Bump and Davis, 2002),  
401        prior to the emplacement of the Trachyte Mesa intrusion. Phase 1 deformation structures  
402        appear to have a preferred ENE–WSW trend, although regional analysis reveals a wider  
403        spread of orientations, which imply a complicated pre-intrusion deformation history, or that  
404        early deformation in the sedimentary cover may have been controlled locally by underlying  
405        basement trends (Bump and Davis, 2002).

406

407                *7.1.2. Phase 2 – Syn-emplacment deformation*

408 Strong spatial, geometric and kinematic relationships between the Phase 2 structures and  
409 the intrusion margin lead to the interpretation (cf. Morgan et al., 2008) that this  
410 deformation is related to the emplacement of the Trachyte Mesa intrusion.

411

412 The relative timings of Phase 2 deformation structures may be further defined through their  
413 cross-cutting relationships: Phase 2B faults and ladder zones overprint the more widespread  
414 2A deformation bands. We suggest that this is a result of strain localisation within the  
415 overburden during vertical inflation of the underlying sill sheet. The observed monoclinial  
416 geometry, and distribution and style of deformation, matches closely to mechanical models  
417 of steeply dipping forced folds (Withjack et al., 1990; Johnson and Johnson, 2002). As  
418 outlined for traverse TMTW (Fig. 7), Phases 2A and 2B deformation appear to alternate as  
419 you move across each individual sill sheet termination. We therefore interpret this to  
420 indicate that this 2A–2B strain localisation may be related to the emplacement of each  
421 individual sheet rather than the overall intrusion.

422

### 423 *7.1.3. Phase 3 – Late-stage emplacement deformation*

424 Phase 3 opening ‘Mode 1’ joints consistently overprint all other structures in the study area.  
425 Phase 3 tensile joints are interpreted to represent late-stage emplacement deformation,  
426 rather than post-emplacement deformation. The joints are most likely associated with  
427 deflation of the host rocks as the magma body beneath cooled, crystallised and contracted.  
428 During vertical inflation of the intrusive sill sheets and overall intrusion, vertical stresses are  
429 exerted on the overriding strata. Following cessation of magma flow and contraction of the  
430 sheets, this stress is removed, and the overriding host rocks relax and tensile joints  
431 (relaxation cooling joints) open. This origin for the Phase 3 joints fits with their wide spatial

432 distribution over the intrusion, in contrast to the Phase 2B faults, which are localised around  
433 sill sheet terminations. A late-stage emplacement timing for the formation of the joints,  
434 rather than post-emplacement, is supported by the presence of calcite crystals on the joint  
435 surface (Fig. 5g) and 'flame-like', fluid escape structures (Fig. 5h) observed on the top  
436 surface of some intrusive sheets, suggesting that these joint sets must have developed while  
437 hydrothermal fluids associated with the intrusion were still circulating.

438

### 439 *7.2. Modes of Emplacement*

440 Davis (1925) first proposed a model for a protolaccolith spreading to its full lateral extent as  
441 a thin sheet before vertical inflation. Hunt (1953) proposed two end-member models  
442 ("bulldozing" and "two-stage growth") for laccolith emplacement and growth from a central  
443 feeder system. In his general description of the emplacement and growth of laccoliths, Corry  
444 (1988) clearly favoured a "two stage growth" model (i.e. radial growth to full lateral extent,  
445 followed by vertical growth) and stated that there is no reported field evidence for the  
446 remnant hinge zones expected for a radial growth model. Koch et al. (1981), Jackson and  
447 Pollard (1988, 1990), Kerr and Pollard (1998) and others suggested that the radial extent of  
448 the intrusion may be controlled by the effective thickness of the overburden and the elastic  
449 properties of the overlying sandstone. However, as discussed by Corry (1988), other factors  
450 such as magma viscosity, strain rate and sheet thickness should also be considered.  
451 Although the models of Hunt (1953) and Corry (1988) refer to the emplacement and growth  
452 of laccoliths, the concepts are just as applicable to a small sill sheet as they are for larger  
453 tabular intrusive bodies.

454



455 Corry (1988) made predictions on the likely deformation associated with Hunt's (1953)  
456 emplacement models, suggesting that deformation associated with a "bulldozing  
457 mechanism" (i.e. radial growth of a full thickness intrusive body) will likely be more complex  
458 and distributed than in the "two-stage growth" model. As magma "bulldozes" its way  
459 through the host rock, it leaves in its wake a series of remnant deformation "hinge zones"  
460 that reflect the propagating deformation front. In contrast, with a "two-stage growth"  
461 model, most of the deformation is localised within the high-strain hinge zones at the lateral  
462 termination. This is because only minor deformation occurs with the initial radial growth of  
463 a thin sheet, and more intense strain developing during the secondary inflation / vertical  
464 growth stage.

465

466 The kinematics and spatial distribution of these deformation structures may therefore be  
467 closely related to the mode of emplacement. Thus deformation is either focused in the area  
468 around the periphery of an intrusion, and is less pronounced in the roof zone above the  
469 intrusion (Corry, 1988), or, as in the classic beam-bending model for a domal intrusion  
470 (Pollard and Johnson, 1973; Kerr and Pollard, 1998), tensile deformation is likely to be  
471 distributed across the wider roof area due to flexure.

472

473 At Trachyte Mesa, our study has demonstrated that the host-rock deformation structures  
474 are strongly localised in the region at the lateral margin of the intrusion, an observation that  
475 confirms previous studies of others (Koch et al., 1981; Corry, 1988; Morgan et al., 2008).  
476 Although thermal alteration and compaction are apparent in host-rock exposures on the  
477 roof of the intrusion, brittle deformation structures such as those described herein on the  
478 NW margin are not observed above the intrusion. This, and the fact that there is no

479 evidence for remnant hinge zones formed by an outward propagating intrusion margin,  
480 would suggest that Trachyte Mesa is likely to have formed by “two-stage” growth. The term  
481 “punched laccolith” (first used by Gilbert, 1877) has been used to describe relatively flat-  
482 topped tabular intrusions, a common characteristic of many laccoliths (including Trachyte  
483 Mesa; Morgan et al., 2008), which have formed through two-stage growth. Corry (1988)  
484 suggested that deformation / accommodation structures associated with a “bulldozing  
485 mechanism” for emplacement are likely to be compression-dominated. In contrast,  
486 extension-dominated deformation and accommodation structures are predicted to occur  
487 with a “two-stage” / incremental vertical growth mechanism. As all of the emplacement-  
488 related deformation structures observed in this study reflect overall extensional strain, our  
489 model for emplacement clearly favours the “two-stage” emplacement mechanism.

490

491 Morgan et al. (2008) proposed an incremental growth model for the Trachyte Mesa  
492 intrusion, through vertical and horizontal growth by the accumulation of multiple horizontal  
493 magma sheets. Their emplacement model has strong similarities to the hybrid case of Corry  
494 (1988), as both include vertical stacking and lateral sheet propagation (and an outward  
495 propagating hinge). In their model, a series of stacked sill sheets are emplaced, with newer  
496 sheets emplaced on top of older. This vertical stacking leads to uplift and monoclinial  
497 bending of the overlying sandstone units, while in front of the sill sheet terminations a low-  
498 pressure triangular-shaped zone develops. Key to the development of this low-pressure  
499 zone is the contrasting rock properties of the thinly bedded shaley units (i.e. more  
500 deformable) along which the sills are emplaced, and the mechanically strong (and more  
501 resistant to bending) overlying massive sandstones (e.g. Fig. 2d). It was envisaged that  
502 tongue-like magma sheets would then fill this low-pressure zone, with this process

503 subsequently leading to lateral propagation of the intrusion (and also the outward  
504 propagation of a deformation hinge).

505

506 The observations presented here are consistent with an incremental, “stacked sill sheet”  
507 growth model for the overall intrusion (cf. Morgan et al., 2008). However, in contrast to that  
508 interpretation, evidence for a “two stage” incremental growth mechanism is observed for  
509 the emplacement of individual sheets. Furthermore, although contrasting styles of  
510 deformation may be observed in the shaley and more massive red sandstone host rock  
511 units, no strong evidence exists for incremental lateral sill propagation. Instead we envisage  
512 that individual sill sheets were emplaced close to their full radial extent as thin sheets that  
513 then vertically inflated through additional magma influx.

514

### 515 *7.3. Emplacement and structural evolution*

516 Based on the work of previous authors (Corry, 1988; Morgan et al., 2008; Thompson and  
517 Schofield, 2008) and our new field observations of intrusion geometries and deformation  
518 structures on the NW margin, a new multistage model for the emplacement of Trachyte  
519 Mesa intrusion is proposed. This emplacement model is shown in Fig. 12 and discussed in  
520 the following sections.

521

#### 522 *7.3.1. Stage 1 - Onset of sheet emplacement and radial growth of a thin “proto-sill”* 523 *sheet*

524 A magma feeder system propagated vertically through the sedimentary pile until it reached  
525 a suitable interval for a horizontal sheet to propagate laterally. In the case of Trachyte Mesa  
526 this is a thin, mechanically weak, reddish-brown silty sandstone and shale layer occurring

527 between thicker, massive sandstone units (Fig. 5b; Morgan et al., 2008). The “proto-sill”  
528 propagated as a thin sheet, with minor inflation, to its maximum lateral extent (Fig. 12). In  
529 contrast, Morgan et al. (2008) suggested that lateral sill propagation and thickening may  
530 have been episodic [i.e. similar to the hybrid model of Hunt (1953) and Corry (1988)].  
531 However, the lack of observable remnant deformation hinge zones on the roof of the  
532 intrusion (and others like it; Corry, 1988) favours propagation of a thin proto-sill sheet  
533 rather than one with significant inflation. The lateral extent of the sill was likely governed by  
534 viscosity of the magma and the properties of the host rock (Thompson and Schofield, 2008).

535

536 Deformation associated with this early emplacement is likely to have been minor, and  
537 dominated by shear at the proto-sill sheet contacts (e.g. stretched plagioclase feldspars; Fig.  
538 11). As magma flowed in a NE direction, spreading out radially to the NW and SE, shear  
539 zones were set up on the top and base surfaces of the intrusion and its contact with the  
540 surrounding host rock. These shear structures are likely to show both brittle and plastic  
541 deformation characteristics due to the effects of hot magma being emplaced into a cold  
542 host rock. Vergence on these shear structures will be opposite to the flow direction of the  
543 magma sheet (i.e. on the NW margin, top-to-the-SE-verging shear fabrics occur on the top  
544 surface of the intrusion). These shear fabrics may be seen both at outcrop and in thin  
545 section (Fig. 11), and have also been defined by AMS (Anisotropy of Magnetic Susceptibility)  
546 studies (Morgan et al., 2008). Shear at the intrusion margin is likely to be the first  
547 accommodating structure related to the onset of sheet emplacement.

548

549 *7.3.2. Stage 2 - Vertical inflation of sill sheet*

550 Once the magma had reached its maximum radial extent, vertical inflation commenced as  
551 magma supply continued. The thickness of the sill will be governed by the thickness of the  
552 overburden (i.e. lithostatic pressure) and the magma pressure (Corry, 1988; Thompson and  
553 Schofield, 2008). Thickening of the sill sheet resulted in roof uplift and deformation (e.g.  
554 forced folding and fracturing) of the overlying strata This is manifest as conjugate sets of  
555 extensional cataclastic deformation band structures (Phase 2A; Figs 4–6), formed in the  
556 overlying massive sandstone beds, localised to the developing lateral margin, increasing in  
557 intensity around the monoclinal flank above the sill termination (Figs 7, 8, 12).

558

559 Although lateral propagation of the sill is likely to have ceased during this inflation phase of  
560 emplacement, shear structures still continued to develop on the top surface of the intrusion  
561 as magma flowed along the sill. In order to accommodate the additional volume of magma,  
562 shear strain on the top surface will have become more dominated by flattening (vertical  
563 shortening).

564

565 As vertical inflation continued strain became localised at the sill sheet termination resulting  
566 in the formation of Phase 2B structures (Figs 6, 12). This strain localisation led to the  
567 development of: first, steep deformation corridors cross-cutting earlier conjugate  
568 deformation bands (Fig. 6c); and second, the development of principal slip surfaces and  
569 ultimately dip-slip faults (Figs 6, 9, 12). These Phase 2B dip-slip faults observed at Trachyte  
570 Mesa therefore played a significant role in accommodating the extra volume of magma  
571 within the crust.

572

573 In the emplacement model of Morgan et al. (2008), sill sheets intruded along a thinly  
574 bedded muddy red sandstone and shale unit as full thickness (~1-5 m thickness) tongue-  
575 shaped sheets with “bulbous” terminations. A temporary zone of low-pressure was created  
576 in front of the intrusion margin as the angle between the stronger massive red sandstone  
577 and the weaker silty sandstone and shale unit beneath increased during vertical growth of  
578 the intrusion through the accumulation of stacked sheets. In this scenario, magma pressure  
579 exceeds lithostatic load, and tongue-like sheets, fed from the stacked sheets, fill the zone of  
580 low-pressure, continuing lateral propagation of the intrusion. However, this explanation is  
581 inconsistent with the structural evidence, as a zone of low-pressure is unlikely to develop  
582 where normal faults accommodate the strain. Instead, it is suggested here that the smooth,  
583 curved nature of the “bulbous” sill sheet terminations (Fig. 3a) are the result of inflation  
584 (akin to that of the rounded surface of a balloon; Fig. 12a). Had this rounded geometry  
585 formed during the sill propagation, there should be more evidence for magma infiltrating  
586 the host rock in front of the intrusion, rather than the presence of sheared, steeply-dipping,  
587 shaley red sandstone.

588

### 589 *7.3.3. Stage 3 - Emplacement of additional sill sheets*

590 Successive sheets were emplaced through the same two-stage emplacement (i.e. radial  
591 followed by vertical growth) as for the first sill sheet. Along structural transect TMTW (Fig.  
592 7), the sequence of sill sheet stacking largely appears to have occurred from the bottom of  
593 the intrusion upwards, as each successive sill sheet was emplaced on top of the underlying  
594 sheet, and hence creating a ‘Christmas-tree’-type laccolith. However, the sequence and  
595 level at which successive sheets were emplaced varies significantly (the impact of out-of-  
596 sequence stacking is discussed below).

597

598           7.3.4. *Stage 4 - Onset of sill-climbing*

599   Following the formation of Phase 2B faults during the vertical inflation stage, magma was  
600   able to utilise these faults and sill-climbing commenced (Figs 12, 13; Thompson and  
601   Schofield, 2008). If the fault plane was able to open, magma was able to propagate along  
602   the fault (Figs 3b, 12, 13). At Trachyte Mesa, examples of sill climbing can be observed at  
603   both outcrop (Fig. 3b) and in thin section (Fig. 10b). This sill climbing preferentially exploited  
604   reverse dip-slip faults (Figs 3b, 13). There are two likely reasons for the magma  
605   preferentially exploiting these faults. The first is that the geometry of the reverse faults,  
606   dipping towards the sill termination, allowed the magma to continue its outward radial flow  
607   up along the fault plane and up through the host stratigraphy. However, probably the most  
608   important factor controlling sill climbing along these faults is the stresses induced on the  
609   fault due to roof uplift (Fig. 13). If the Phase 2B faults have a normal geometry (i.e. dipping  
610   away from the sill sheet), compressional forces, due to both uplifting of the roof strata and  
611   loading of the overburden, keep the plane closed and prevent migration of magma along its  
612   path (Fig. 13). In contrast, if the fault has a reverse geometry (i.e. dipping towards the sill  
613   sheet), roof uplift forces reduce the vertical stress on the fault, thus enabling magma to  
614   exploit the fault plane (Fig. 13).

615

616           7.3.5. *Stage 5 - Cooling and relaxation of intrusion*

617   As the intrusive sheets (and overall intrusive body) started to cool and contract with the  
618   cessation of magma flow, the host rocks above also relaxed. During this relaxation of the  
619   overriding strata, and the removal of the vertical compressive stresses that had been

620 exerted on the overlying sediments during vertical inflation of the intrusive sheets, tensile  
621 joints formed and opened, allowing hydrothermal fluids to circulate (Figs 5g, h, 12).

622

#### 623 *7.4. Sequence of stacking*

624 The sequence in which intrusive sill sheets are stacked plays a significant role in the resulting  
625 geometry of the intrusion and the overlying stratigraphy, as well as the types of  
626 deformation structures observed in the host rocks. In the two structural transects carried  
627 out here (Figs 2, 7, 8), two contrasting styles of intrusion geometry are observed that appear  
628 to be the result of different orders of sill stacking. In TMTW, the margin of the intrusion is  
629 characterised by a series of sub-horizontal sill sheets of varying thickness (1.5 m) stacked  
630 one on top of the other (Fig. 7). This conventional stacking sequence would be consistent  
631 with the order of stacking discussed above and outlined in Fig. 12a. In contrast, in TMTE the  
632 order of sill stacking appears out-of-sequence. As discussed by Morgan et al. (2008) and  
633 highlighted in Fig. 8b, it appears that the lower sub-horizontal sheets were actually  
634 emplaced later than upper sheets. The main evidence for this out-of-sequence stacking is  
635 the fact that the upper sill sheets have been arched and rotated upwards in a similar  
636 monoclinial geometry to the overlying sandstone beds due to the emplacement of sub-  
637 horizontal sheets beneath.

638

639 Not only does the sequence of stacking affect the geometry of the intrusion, it also has a  
640 significant impact on the style of deformation occurring in the overriding host rock  
641 (compare Figs 7, 8). In a sequentially stacked sequence (e.g. TMTW; Fig. 7) a “stepped”  
642 bedding profile is developed (i.e. terraces associated with individual sill sheets), and dip-slip  
643 faults (Phase 2B) occur at the tips of successive intrusive sheets. In areas where out-of-



644 sequence emplacement is apparent (e.g. TMTE; Fig. 8), the intrusion margin is distinctly  
645 monoclinal (i.e. one single step), and due to the presence of the overriding sill sheets,  
646 development of Phase 2B faults is inhibited (Fig. 12b). Close to the intrusion contact,  
647 compressional deformation structures including small reverse faults are observed, although  
648 in the more competent sandstone beds extension-dominated deformation structures still  
649 prevail (Fig. 5b).

650

#### 651 *7.5. Faulting at sill terminations*

652 A significant observation from this study, previously undocumented at Trachyte Mesa, is the  
653 presence of dip-slip faults associated with individual sill terminations (i.e. Phase 2B  
654 structures). Thompson and Schofield (2008) suggested that the main control on the  
655 development of faults at sill sheets terminations is the depth of formation. At shallower  
656 depths, cohesive strength along bedding planes is less, and so favours the development of  
657 flexural slip folding. As depth increases, higher shear stresses are required for flexural slip,  
658 thus favouring mechanical failure of the rock through fracture / faulting (Stearns, 1978).

659

660 Pollard and Johnson (1973) presented a conceptual model for the formation of peripheral  
661 dykes located at the tips of laccolith bodies from field observations. It was suggested that  
662 the dykes formed at the periphery of the intrusions as a result of flexural / elastic bending of  
663 the overburden layers (contractional over the centre and extensional over the periphery).  
664 Evidence for sill-climbing at Trachyte Mesa is in agreement with such extensional strain at  
665 the periphery. However, instead of the strain being accommodated by simple opening  
666 'Mode 1' joints, it is proposed that it was the Phase 2B faults that were exploited by the  
667 magma (Fig. 3b).

668

669 Sill climbing associated with the exploitation of periphery faults is likely to play a significant  
670 role in the development of saucer-shaped sills (Galland et al., 2009; Fig. 13). Thompson and  
671 Schofield (2008) took this process a stage further, with the flow pathway of the magma  
672 flattening again at some point along the fault plane. This stage has not been observed in  
673 exposures at Trachyte Mesa.

674

#### 675 *7.6. Micro-Macro emplacement structures*

676 Intrusions and their associated deformation are typically scalar-invariant in nature  
677 (McCaffrey and Petford, 1997). Although it has not been a major focus of this study, it is  
678 worthy of note that multiple examples of similar deformation structures occur at both the  
679 outcrop and microstructural scales. Examples of this include the steeply dipping, Phase 2b  
680 dip-slip faults and shear planes at the tips of intrusive sheets (Figs. 6d, e, 10), propagation of  
681 magma along faults (Figs 5h, 10b), Riedel shears associated with shearing on the top surface  
682 of the intrusion (Fig. 11), as well as the consistent two-stage growth mechanism for both  
683 individual sheets and the entire intrusion. The structural similarities we observe at multiple  
684 scales (i.e. thin section, individual intrusive sheets and the overall intrusion) may reflect a  
685 scale-invariance which may make our models applicable to larger-scale intrusions (i.e.  
686 laccoliths and plutons; cf. Rocchi et al., 2002).

687

### 688 **8. Conclusions**

689 Trachyte Mesa intrusion, the most distal satellite intrusion of the Mount Hillers intrusive  
690 complex in the Henry Mountains Utah, comprises a series of stacked sill sheets.  
691 Deformation structures (geometry, kinematics, spatial distribution) associated with the

692 emplacement of the intrusion vary in style and intensity along the intrusion margin. Detailed  
693 analysis of the host rock deformation structures and their cross-cutting relationships  
694 enables the recognition of three distinct phases, interpreted to represent pre- (Phase 1),  
695 syn- (Phase 2), and late-stage (Phase 3) emplacement deformation stages. Spatial and  
696 kinematic association of Phase 2 structures (deformation bands and dip-slip faults) indicate  
697 extensional strain normal to the intrusion margin during emplacement, with the inclination  
698 of the sigma-3 axis reflecting the flexural nature of the margin.

699

700 The preferred emplacement model of a series of stacked sill sheets is in agreement with  
701 previous studies (Morgan et al., 2008), but a different mechanism for the emplacement of  
702 individual sill sheets is envisaged in which dip-slip faults accommodate sill inflation / vertical  
703 growth. All emplacement-related deformation structures observed reflect extensional  
704 strain-dominated deformation. Each individual sill sheet is believed to have grown to its  
705 maximum radial extent as a thin sheet, and then in a second stage, to inflate vertically to its  
706 present thickness. It is likely that most deformation of the host rock took place during this  
707 second stage, with faults developing at the sill terminations due to strain localisation.

708

709 Magma preferentially exploited the faults that developed at the periphery of sill sheets,  
710 initiating sill climbing. Extensional roof faulting and sill climbing support a two-stage growth  
711 history for the overall intrusion. These observations are consistent with theoretical models  
712 of sill emplacement (e.g. Pollard and Johnson, 1973; Koch et al., 1981; Thompson and  
713 Schofield, 2008).

714

715 The order in which sill sheets are stacked has impacted the intrusion geometry and  
716 associated deformation. In conventionally stacked sequences (i.e. base upwards) a  
717 “stepped” / terraced bedding profile develops, with the presence of dip-slip faults localised  
718 at the tips of successive intrusive sheets. By contrast, where intrusive sheets are emplaced  
719 beneath earlier intruded sheets (i.e. out-of-sequence stacking), the resulting intrusion and  
720 host rock geometries and emplacement-related deformation structures are significantly  
721 different, having a monoclinical rather than stepped profile, with no dip-slip faults at sill  
722 terminations.

723

724 Not only do the deformation structures record the strain evolution, and thus mode of  
725 emplacement of the intrusion, they also controlled the subsequent propagation of the  
726 intrusive body (e.g. in the form of sill climbing). These observations provide new insights on  
727 the emplacement mechanisms of sills and laccoliths, how magma is accommodated in the  
728 subsurface and how emplacement of high level intrusions can affect sedimentary host rocks.

729

### 730 **References**

731 Aydin, A., 1978. Small faults formed as deformation bands in sandstone. *Pure and Applied*  
732 *Geophysics*, 116, 913–930.

733 Aydin, A. and Johnson, A.M., 1978. Development of faults as zones of deformation bands  
734 and as slip surfaces in sandstones. *Pure and Applied Geophysics*, 116, 931–942.

735 Aydin, A. and Johnson, A.M., 1983. Analysis of faulting in porous sandstones. *Journal of*  
736 *Structural Geology*, 5, 19–31.

737 Bump, A.P. and Davis, G.H., 2003. Late Cretaceous – early Tertiary Laramide deformation of  
738 the northern Colorado Plateau, Utah and Colorado. *Journal of Structural Geology*, 25, 421–  
739 440.

740 Coleman, D.S., Gray, W. and Glazner, A.F., 2004. Rethinking the emplacement and evolution  
741 of zoned plutons: geochronologic evidence for incremental assembly of the Tuolumne  
742 Intrusive Suite, California. *Geology*, 32, 433–436.

743 Corry, C.E., 1988. *Laccoliths: Mechanics of Emplacement and Growth*. Geological Society of  
744 America, Special Papers, 220, 110 pp.

745 Cruden, A.R. and McCaffrey, K.J.W., 2001. Growth of plutons by floor subsidence:  
746 implications for rates of emplacement, intrusion spacing and melt-extraction mechanisms.  
747 *Physics and Chemistry of the Earth Part A: Solid Earth & Geodesy*, 26, 303–315.

748 Davis, G.H., 1978. Monocline fold pattern of the Colorado Plateau. In: Matthews, V.I. (Ed.),  
749 *Laramide Folding Associated with Basement Block Faulting in the Western United States*.  
750 Geological Society of America Memoir, 151, pp. 215–233.

751 Davis, W.M., 1925. Laccoliths and sills (abs.). *Washington Academy of Science Journal*, 15,  
752 414–415.

753 Davis, G., 1999. Structural geology of the Colorado Plateau region of southern Utah, with  
754 special emphasis on deformation bands. Geological Society of America, Special Papers, 342.

755 Du Toit, A.L., 1920. The Karoo dolerites of South Africa: a study in hypabyssal injection.  
756 *Transactions of the Geological Society of South Africa*, 23, 1–42.

757 Engel, C.G., 1959. Igneous rocks and constituent hornblendes of the Henry Mountains, Utah.  
758 *Geological Society of America Bulletin*, 70, 951-980. DOI: 10.1130/0016-  
759 7606(1959)70[951:IRACHO]2.0.CO;2.

760 Fossen, H., Schultz, R.A., Shipton, Z.K. and Mair, K., 2007. Deformation bands in sandstone: a  
761 review. *Journal of the Geological Society London*, 164, 755–769. DOI: 10.1144/0016-  
762 76492006-36.

763 Galland, O., Planke, S., Neumann, E.-R. and Malthé-Sørensen, A., 2009. Experimental  
764 modelling of shallow magma emplacement: application to saucer-shaped intrusions. *Earth  
765 and Planetary Sciences Letters*, 277, 373–383. DOI: 10.1016/j.epsl.2008.11.003

766 Gilbert, G.K., 1877. *Geology of the Henry Mountains, Utah*. U.S. Geographical and Geological  
767 Survey of the Rocky Mountain Region, 170 pp.

768 Gilbert, G.K., 1896. Laccolites in southeastern Colorado. *Journal of Geology*, 4, 816–825.

769 Glazner, A.F., Bartley, J.M., Coleman, D.S., Gray, W. and Tayler, R.Z., 2004. Are plutons  
770 assembled over millions of years by amalgamation from small magma chambers? *GSA  
771 Today*, 14. doi: 10.1130/1052-5173(2004)013!0004:APAOMOO.

772 Habert, G. and de Saint-Blanquat, M., 2004. Rate of construction of the Black Mesa  
773 bysmalith, Henry Mountains, Utah, USA. In: Bretkreutz, C. and Petford, N. (eds.) *Physical  
774 geology of high-level magmatic systems*. Geological Society, London, Special Publication,  
775 234, 143–159.

776 Horsman, E., Tikoff, B. and Morgan, S., 2005. Emplacement related fabric in a sill and  
777 multiple sheets in the Maiden Creek sill, Henry Mountains, Utah. *Journal of Structural  
778 Geology*, 27, 1426–1444. doi:10.1016/j.jsg.2005.03.003.

779 Hunt, C.B., 1953. *Geology and Geography of the Henry Mountains Region, Utah*. U.S.  
780 Geological Survey Professional Paper, 228, 234 pp.

781 Hunt, C.B., 1988. *Geology of the Henry Mountains, Utah, as recorded in the notebooks of  
782 G.K. Gilbert, 1875-1876*. Geological Society of America Memoir, 167, 229 pp.

783 Hutton, D.H.W., 1996. The 'space problem' in the emplacement of granite. *Episodes, Journal*  
784 *of International Geoscience*, 19, no 4, 114–119.

785 Hutton, D.H.W., 1997. Syntectonic granites and the principle of effective stress: a general  
786 solution to the space problem? In: Bouchez, J.L., Hutton, D.H.W., and Stephens, W.E., (Eds.),  
787 *Granite: from segregation of melt to emplacement fabrics. Petrology and Structural*  
788 *Geology*, 8, 189–197. DOI: 10.1007/978-94-017-1717-5\_12

789 Jackson, S.E., and Pollard, D.D., 1988. The laccolith-stock controversy: New results from the  
790 southern Henry Mountains, Utah. *Geological Society of America Bulletin*, 100, 117–139.  
791 doi:10.1130/0016-7606.

792 Jackson, S.E., and Pollard, D.D., 1990. Flexure and faulting of sedimentary host rocks during  
793 growth of igneous domes, Henry Mountains, Utah. *Journal of Structural Geology*, 12, 185–  
794 206, doi:10.1016/0191-8141(90)90004-I.

795 Johnson, A.M., and Pollard, D.D., 1973. Mechanics of growth of some laccolithic intrusion in  
796 the Henry Mountains, Utah, I: Field observations, Gilbert's model, physical properties and  
797 flow of the magma. *Tectonophysics*, 18, 261–309, doi:10.1016/0040-1951(73)90050-4.

798 Johnson, K.M., and Johnson, A.M., 2002. Mechanical analysis of the geometry of forced-  
799 folds. *Journal of Structural Geology*, 24, 401–410.

800 Kerr, A.D., Pollard, D.D., 1998. Towards more realistic formulations for the analysis of  
801 laccoliths. *Journal of Structural Geology*, 20, 1783–1793.

802 Koch, F.G., Johnson, A.M., and Pollard, D.D., 1981. Monoclinial bending of Strata over  
803 laccolithic intrusions. *Tectonophysics*, 74, T21–T31.

804 Larson M.J, Bromfield C.S., Dubiel R.F., Patterson C.G. and Peterson F., 1985. Geologic map  
805 of the Little Rockies wilderness study area and the Mt. Hillers and Mt. Pennell study areas,  
806 and vicinity, Garfield County, Utah. U.S. Geological Survey Map MF-1776-B.

807 Magee, C., Stevenson, C. T., O'Driscoll, B. and Petronis, M., 2012. Local and regional controls  
808 on the lateral emplacement of the Ben Hiant dolerite intrusion, Ardnamurchan (NW  
809 Scotland). *Journal of Structural Geology*, 39, 66–82. doi.org/10.1016/j.jsg.2012.03.005

810 Mahan, K.H., Bartley, J.M., Coleman, D.S., Glazner, A.F. and Carl, B., 2003. Sheeted intrusion  
811 of the synkinematic McDoogle pluton, Sierra Nevada, California. *Geological Society of  
812 America Bulletin*, 115, 1570–1582. McCaffrey, K.J.W. and Petford, N., 1997. Are granitic  
813 intrusions scale invariant? *Journal of the Geological Society London*, 154, 1–4.

814 Petford, N., Cruden, A.R., McCaffrey K.J.W. and Vignerosse, J.L., 2000. Granitic magma  
815 formation, transport and emplacement in the Earth's Crust. *Nature*, 408, 669–673

816 Morgan, S., Horsman, E., Tikoff, B., de Saint Blanquat, M., Nugent, A. and Habert G., 2005.  
817 Sheet-like emplacement of satellite laccoliths, sills and bysmaliths of the Henry Mountains,  
818 southern Utah. In: Pederson J. and Dehler, C.M. (Eds.), *Interior Western United States Field  
819 Guide*, GSA Field Guides, 6, 283–309. doi: 10.1130/2005.fld006(14)

820 Morgan, S., Stanik, A., Horsman, E., Tikoff, B., de Saint Blanquat, M. and Habert., G., 2008.  
821 Emplacement of multiple magma sheets and wall rock deformation: Trachyte Mesa  
822 intrusion, Henry Mountains, Utah. *Journal of Structural Geology*, 30, 491–512,  
823 DOI:10.1016/j.jsg.2008.01.005.

824 Nelson, S.T., Davidson, J.P. and Sullivan, K.R., 1992. New age determinations of central  
825 Colorado Plateau laccoliths, Utah: Recognizing disturbed K–Ar systematics and re-evaluating  
826 tectonomagmatic relationships. *Geological Society of America Bulletin*, 104, 1547–1560.



827 Nelson, S.T. and Davidson, J.P., 1993. Interactions between mantle-derived magmas and  
828 mafic crust, Henry Mountains, Utah. *Journal of Geophysical Research B2*, 98, 1837–1852.

829 Pitcher, W.S., 1970. Ghost stratigraphy in intrusive granites: a review. In: Newall, G. and  
830 Rast, N. Eds.), *Mechanism of Igneous Intrusion*, Liverpool, Gallery Press, 123–140.

831 Pollard, D.D. and Johnson, A.M., 1973. Mechanics of growth of some laccolithic intrusions in  
832 the Henry Mountains, Utah, II: bending and failure of overburden layers and sill formation.  
833 *Tectonophysics*, 18, 261–309.

834 Pollard, D.D., Muller, O.H. and Dockstader, D.R., 1975. The form and growth of fingered  
835 sheet intrusions. *Geological Society of America Bulletin*, 3, 351–363.

836 Pollard, D.D., 1987. Elementary fracture mechanics applied to the structural interpretation  
837 of dykes. In: Halls, H.C. and Fahrig, W.F. (Eds.) *Mafic Dyke Swarms*. Geological Association of  
838 Canada, Special Paper, 34, 5–24.

839 Reches, Z., 1987. Determination of the tectonic stress tensor from slip along faults that obey  
840 the Coulomb yield condition. *Tectonics*, 6, 849–861

841 Rocchi, S., Westerman, D.S., Dini, A., Innocenti, F. and Tonarini, S., 2002. Two-stage laccolith  
842 growth at Elba Island (Italy). *Geology*, 30, 983–986.

843 Saint Blanquat, M. (de) and Tikoff, B., 1997. Development of magmatic to solid-state fabrics  
844 during syntectonic emplacement of the Mono Creek Granite, Sierra Nevada Batholith. In:  
845 Bouchez, J.L., Hutton, D.H.W, Stephens, W.E. (Eds.), *Granite: From Segregation of Melt to*  
846 *Emplacement Fabrics*. Kluwer Academic Publishers, Dordrecht, 231–252.

847 Saint Blanquat, M. (de), Habert, G., Horsman, E., Morgan, S., Tikoff, B., Launeau, P. and  
848 Gleizes, G., 2006. Mechanisms and duration of non-tectonically, assisted magma

849 emplacement in the upper crust: Black Mesa pluton, Henry Mountains, Utah.  
850 *Tectonophysics*, 428, 1–31, doi:10.1016/j.tecto.2006.07.014.

851 Schofield, N., Stevenson, C. and Reston, T., 2010. Magma fingers and host rock fluidization in  
852 the emplacement of sills. *Geology*, 38, 63–66.

853 Schofield, N.J., Brown, D.J., Magee, C. and Stevenson, C.T., 2012. Sill morphology and  
854 comparison of brittle and non-brittle emplacement mechanisms. *Journal of the Geological*  
855 *Society London*, 169, 127–141.

856 Shipton, Z.K. and Cowie, P.A., 2001. Damage zone and slip-surface evolution over  $\mu\text{m}$  to km  
857 scales in high-porosity Navajo sandstone, Utah. *Journal of Structural Geology*, 23, 1825–  
858 1844.

859 Stevenson, C.T.E., Owens, W.H., Hutton, D.H.W., Hood, D.N. and Meighan, I., 2007a.  
860 Laccolithic, as opposed to cauldron subsidence, emplacement of the Eastern Mourne  
861 pluton: Evidence from anisotropy of magnetic susceptibility: *Journal of Geological Society*  
862 *London*, 164, 99–110. doi: 10.1144/0016076492006-008.

863 Stevenson, C.T.E., Owens, W.H. and Hutton, D.H.W., 2007b. Flow lobes in granite: The  
864 determination of magma flow direction in the Trawenagh Bay Granite, north-western  
865 Ireland, using anisotropy of magnetic susceptibility. *GSA Bulletin*, 119, 1368–1386. doi:  
866 10.1130/B25970.1

867 Thompson, K., 2004. Sill complex geometry and internal architecture: a 3D seismic  
868 perspective. In: Breitkreutz, C. and Petford, N. (eds.) *Physical Geology of High-level*  
869 *Magmatic Systems*. Geological Society London, Special Publication, 234, 229–232.

870 Thomson, K. and Hutton, D., 2004. Geometry and growth of sill complexes: insights using 3-  
871 d seismic from the North Rockall Trough. *Bulletin of Volcanology*, 66, 364–375.

872 Thompson, K. and Schofield, N., 2008. Lithological and structural controls on the  
873 emplacement and morphology of sills in sedimentary basins. In: Thompson, K. and Petford,  
874 N. (Eds.) Structure and Emplacement of High-Level Magmatic Systems. Geological Society  
875 London, Special Publication, 302, 31–44.

876 Tikoff, B., Blenkinsop, T., Kruckenberg, S.C., Morgan, S., Newman, J. and Wojtal, S., 2013. A  
877 perspective on the emergence of modern structural geology: Celebrating the feedbacks  
878 between historical-based and process-based approaches. Geological Society of America  
879 Special Papers, 500, 65–119. doi: 10.1130/2013.2500(03)

880 Westerman, D.S., Dini, A., Innocenti, F. and Rocchi, S. 2004. Rise and fall of a nested  
881 Christmas-tree laccolith complex, Elba Island, Italy. In: Breitzkreuz, C. and Petford, N. (Eds.)  
882 Physical Geology of High-level Magmatic Systems. Geological Society London, Special  
883 Publication, 234, 195–213.

884 Wetmore, P.H., Connor, C.B., Kruse, S.E., Callihan, S., Pignotta, G., Stremtan, C. and Burke A.,  
885 2009. Geometry of the Trachyte Mesa intrusion, Henry Mountains, Utah: Implications for  
886 the emplacement of small melt volumes into the upper crust. *Geochemistry Geophysics*  
887 *Geosystems*, 10, Q08006. DOI: 10.1029/2009GC002469.

888 Wilson, P.I.R. and McCaffrey, K.J.W., 2013. Intrusion space problem: digital mapping and  
889 analysis of the Maiden Creek satellite intrusion, Henry Mountains Utah. *Geoscientist*, 23 (6),  
890 16–19.

891 Wilson, P.I.R., McCaffrey, K.J.W., and Holdsworth, R.E., In Prep. Syn-emplacement  
892 accommodation structures of igneous intrusions: Maiden Creek intrusion, Henry Mountains,  
893 Utah. For submission to *Geosphere*.

894 Withjack, M.O., Olson, J. and Peterson, E., 1990. Experimental models of extensional forced  
895 folds. AAPG Bulletin, 74, 1038–1054.

896

897

## Figure Captions

898

899 **Fig. 1.** Simplified geological maps of the study area. (a) The Henry Mountains region  
900 (adapted from Morgan et al., 2008) and its location within Utah (inset map). (b) Mount  
901 Hillers and its satellite intrusions (modified from Larson et al., 1985). In (b), the various  
902 intrusions that comprise the Mt Hillers intrusive complex are numbered, using the names  
903 given by Hunt (1953) : 1 – Mt Hillers central complex; 2 – Bulldog Peak intrusion; 3 – Stewart  
904 Ridge intrusion; 4 – Specks Ridge intrusion; 5 – Chaparral Hills Laccolith; 6 – Specks Canyon;  
905 7 – speculated feeder system to the Trachyte Mesa intrusion; 8 – Black Mesa intrusion; 9 –  
906 Sawtooth Ridge intrusion; 10 - Maiden Creek intrusion; and 11 – Trachyte Mesa intrusion.

907

908 **Fig. 2.** Location of the study sections. (a) Contoured and georeferenced aerial image of the  
909 Trachyte Mesa area showing the intrusion outline of Morgan et al. (2008). Locations of  
910 structural stations are shown by the blue filled circles. (b) 3D DEM model of the Trachyte  
911 Mesa area, view looking NE. Note viewpoint location for photo (e). (c) Contoured and  
912 georeferenced aerial image of field study area, located on the southern end of the NW  
913 margin of the intrusion. Structural station localities, bedding measurements, structural  
914 transect lines (TMTE, TMTW) and detailed study area (TMT3) are shown. (d) Schematic  
915 cross-sections (NW–SE) across the Trachyte Mesa intrusion, showing stacked sill sheets  
916 (after Morgan et al., 2008). (e) Field photograph showing monoclinial upper contact and  
917 stacked intrusive sheets observed at NW margin of intrusion. Note, zoom in image in (d) is  
918 based on the field observations at this outcrop locality.

919

920 **Fig. 3.** Photographs and interpretative sketches showing outcrop geometries of stacked sill  
921 sheets on the southern NW margin of Trachyte Mesa. (a) View looking SE from station  
922 TMTE-6 along structural transect TMTE. (b) View looking NE from station TMTW-2 onto  
923 structural transect TMTW (foreground). N.B. Structural transect TMTE can be seen in the  
924 background. Key observations to note are: monoclinical geometry of overriding sandstone  
925 units, (a) and (b); flexed / monoclinical upper sill sheets (a) vs. sub-horizontal stacked sill  
926 sheets (b); sub-horizontal lower sill sheets with “bulbous” terminations (a) and (b); sill  
927 climbing in upper sill sheet, propagating along reverse dip-slip fault (b).

928

929 **Fig. 4.** Summary stereoplots of field structural data. Equal area, lower hemisphere  
930 stereoplots of data showing poles to planes (contoured) sorted by structural type: (a)  
931 bedding, (b) deformation bands, (c) faults, (d) opening ‘Mode 1’ joints; and structural phase:  
932 (e) Phase 1, (f) Phase 2A, (g) Phase 2B, (h) Phase 3. Mean planes for distinct cluster  
933 populations are shown for each plot. Plots (c) and (g) also show fault slip lines with  
934 movement direction indicated (solid fill = normal fault slip; white fill = reverse slip).

935

936 **Fig. 5.** Annotated field photographs showing examples of Phase 1 (a), Phase 2 (b–d), and  
937 Phase 3 (e–h) deformation structures. (a) Background deformation bands cutting the  
938 Entrada Sandstone distal to the intrusion (0.2–2m spacing). (b) Deformation structures at  
939 intrusion contact, locality TMTE-9 in Fig. 3. Low angle shear and reverse faults (top-to-the-  
940 SE) on top surface of the intrusion and within the highly deformed shaley red sandstone  
941 layer adjacent to the contact. Extensional conjugate deformation bands in massive red  
942 sandstone (also see fig. 9 in Morgan et al., 2008). (c) Closely spaced porosity reducing

943 deformation bands in massive red sandstone, localised to intrusion margin and host-rock  
944 overlying the top surface of the intrusion (0.5–5cm spacing). (d) Dip-slip normal fault (down-  
945 to-the-NW) with well-preserved slickenlines on principal slip surface. (e) Opening ‘Mode I’  
946 joints trending perpendicular to the intrusion margin (NW–SE), 0.5–2m spacing. (f) Opening  
947 ‘Mode I’ joints trending parallel to the intrusion margin (NE–SW), 1–2m spacing. (g) Calcite  
948 crystals precipitated on margin parallel joint surfaces in (f). (h) Calcite precipitation and  
949 apparent fluid exploitation of joint systems on top surface of intrusion.

950

951 **Fig. 6.** Annotated field photographs showing additional examples of Phase 2A (a–b) and 2B  
952 (c–e) structures and kinematics. (a) Monoclinal bedding geometries in sandstone units ~30  
953 m above the intrusion showing conjugate fault / deformation band geometries consistent  
954 with flexure (note offset on bedding in paler sandstone unit). (b) Outcrop example (~5 m  
955 above intrusion) of conjugate deformation banding showing consistent offsets to those seen  
956 in (a). (c) Steep ladder zone (down-to-the-NW shear) overprinting conjugate deformation  
957 bands. Note kinematics of background deformation bands and ladder zone are the same. (d)  
958 Outcrop example of normal faults developed at the termination of sill sheets. Note, total  
959 throw on normal faults is consistent with the thickness of the individual sill sheet, implying  
960 that the faults may be induced by sill sheet inflation. (e) Zoomed-in area outlined in (d)  
961 showing ~50 cm normal (down-to-the-NW) offset of bedding contact (PSS – Principal Slip  
962 Surface; DZ – Damage Zone).

963

964 **Fig. 7.** Structure along Trachyte Mesa transect TMTW. Cross section (for location see Fig. 2c)  
965 constructed in 2D Move™. Equal area, lower hemisphere plots of poles to planes highlight

966 deformation structure populations collected at each station (white stars; bedding planes  
967 highlighted in yellow). Note the stepped / terraced geometry of the margin. Colour bars  
968 across the lower part of the section show the spatial distribution of the different  
969 deformation phases.

970

971 **Fig. 8.** Structure along Trachyte Mesa transect TMTE. (a) Cross section (for location see Fig.  
972 2c) constructed in 2D Move™. See Fig. 7 for key. Note, the main intrusion is in the SE (to the  
973 right) of the section, while a smaller distal intrusion can be seen further outboard. (b) Close-  
974 up of the area around the intrusion margin and corresponding field photograph of the same  
975 outcrops. Numbers 1–5 indicate the possible timing of sheet emplacement, with 1 being the  
976 earliest sheet. Note the monoclinical geometry of the upper sill sheets and overriding massive  
977 sandstone.

978

979 **Fig. 9.** Field photographs and structural data demonstrating the arcuate trend of Phase 2B  
980 faults. (a), (b) Equal area lower hemisphere stereoplots showing all fault trends of Phase 2B  
981 faults. Faults show dip-slip normal and reverse movements, consistent with NW–SE  
982 extension (note inclination of  $\sigma_3$ , associated with flexure along the intrusion margin).  
983 (c) Map showing the distribution of the main outcrop localities at which Phase 2B fault data  
984 were collected. The change in geometry and kinematics of the faults with the changing  
985 trend of the intrusion margin can be seen from the equal area lower hemisphere plots for  
986 each outcrop showing poles to planes, slickenlines and interpreted kinematics. Solid white  
987 lines depict areas where intrusion margin is exposed in outcrop, dashed white lines show  
988 inferred continuation of margin beneath sandstone beds (note, magnetic data from



989 Wetmore et al. (2009) was used to guide this subsurface geometry). (d) – (f) Field  
990 photographs showing outcrop examples of Phase 2 dip-slip normal faults. Although  
991 individual faults are quite linear, a clear rotation in fault trend may be seen when walking  
992 along strike. Many fault surfaces have well-developed slickenlines showing almost pure dip-  
993 slip kinematics.

994

995 **Fig. 10.** Photomicrographs of microstructures observed at the intrusion – sandstone contact.

996 (a) Stepped vertical contact at the tip of an intrusive sill sheet. (b) Magma injecting upwards  
997 along an extensional fracture. (c) Top surface of intrusion showing sharp contact and narrow  
998 altered margin. (d) Sub-vertical fracture within host rock adjacent to contact, showing  
999 down-to-the-NW movement. (e) Oriented sample highlighting area of thin section and  
1000 location of images (a) – (d).

1001

1002 **Fig. 11.** Flow generated fabrics at the intrusion margin. (a) Outcrop photograph showing

1003 low-angle brittle extensional faults (see inset stereoplot) cutting baked sandstone unit on  
1004 top surface of an intrusive sheet. These are interpreted to be equivalent to R1 Riedel shear  
1005 planes, depicted in (d). The faults are only apparent in the baked sandstone and appear to  
1006 terminate at the intrusion-host rock interface. (b) Stretched plagioclase phenocrysts within  
1007 a strongly sub-horizontal foliated zone (2–3 cm) on the top surface of an intrusive sheet.  
1008 Note also the thin (<1 cm) chilled margin zone above the stretched phenocryst / foliated  
1009 layer. (c) Photomicrograph of deformed, elongate plagioclase phenocryst within the  
1010 uppermost 2–3cm of an intrusive sheet (note section is cut along a vertical plane oriented  
1011 parallel to the stretching direction, 140°–320°). The phenocryst is deformed mainly by brittle

1012 deformation and a series of preferred deformation planes, with offset, can be identified.  
1013 The movement and orientation of these planes are consistent with Riedel fractures  
1014 associated with top-to-the-right (SE) sub-horizontal shear. (d) Schematic cartoon depicting  
1015 the deformation structures observed at outcrop and in thin section on the top surface of an  
1016 intrusive sheet. The structures and kinematics are consistent with top-to-the-SE sub-  
1017 horizontal shear. This shearing is likely driven by magmatic flow within the underlying sheet,  
1018 leading to sub-horizontal shortening and shear at the intrusion contact.

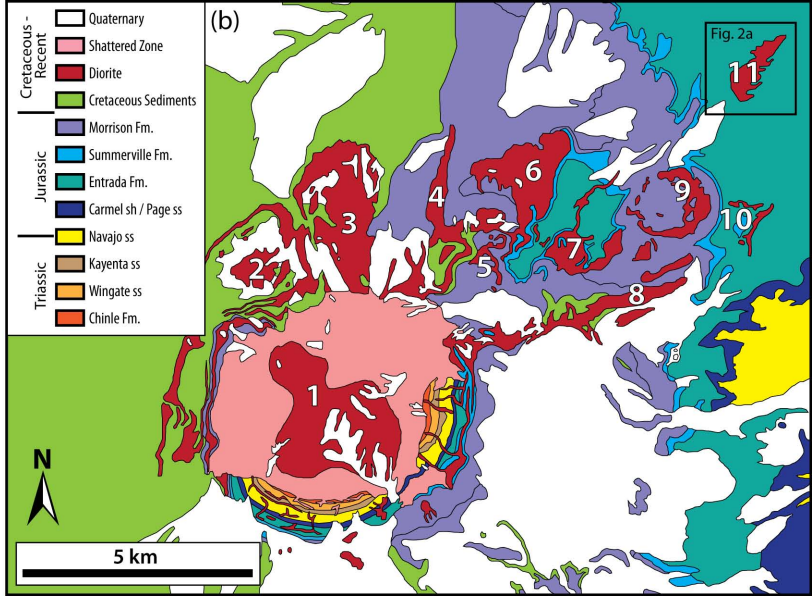
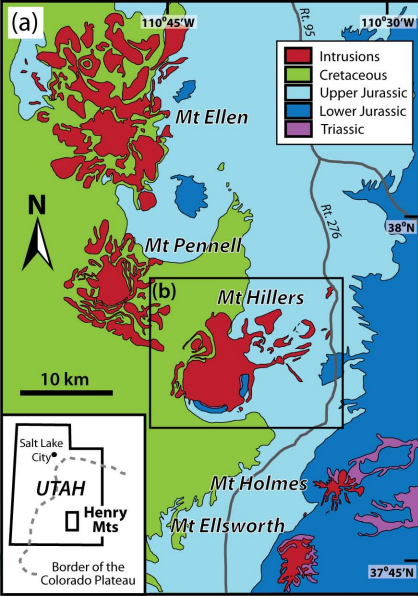
1019

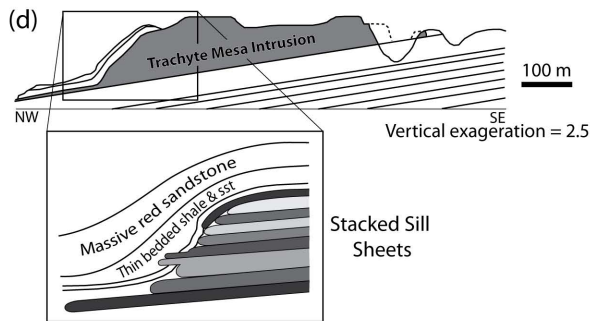
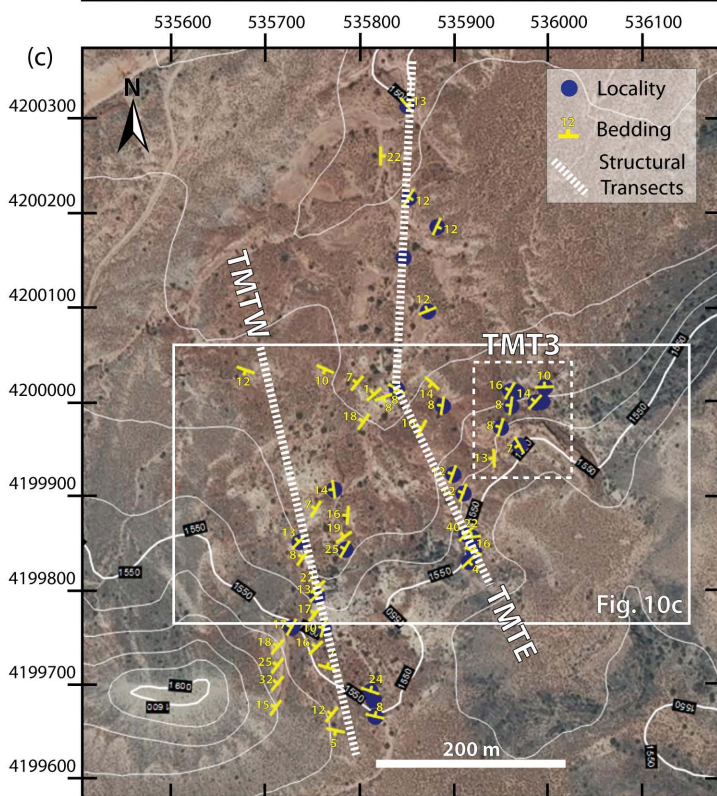
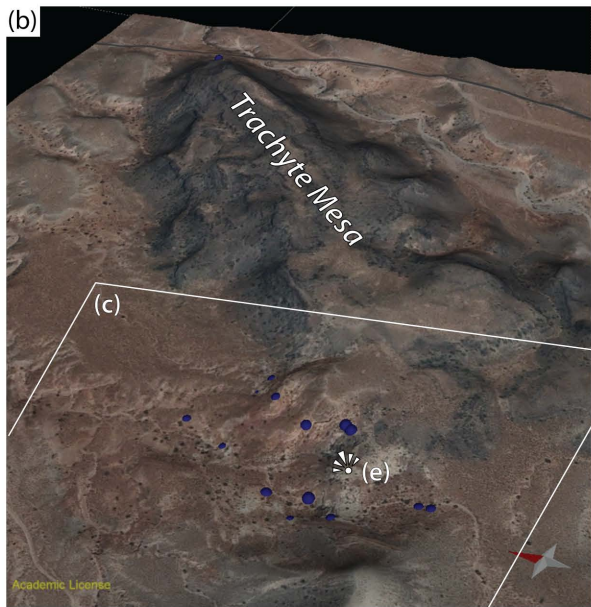
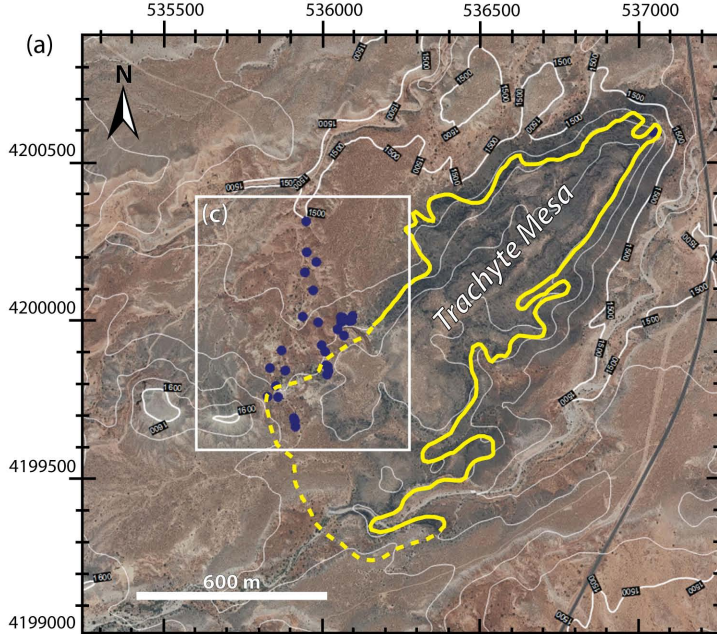
1020 **Fig. 12.** Schematic diagram outlining a two-stage growth model for sill emplacement at the  
1021 Trachyte Mesa intrusion and associated deformation structures. (a) Conventional stacking  
1022 model (as observed at TMTW study area; Fig. 7). Stages of emplacement, as discussed in  
1023 text, are: Stage 1 - Sill initiation and radial growth as a thin “proto-“ sill sheet; Stage 2 -  
1024 Thickening of the sill sheet, resulting in roof uplift and strain localisation in the host rock at  
1025 the sill sheet termination; Stage 3 - Emplacement of a second sill sheet (repetition of stages  
1026 1 and 2 for 2<sup>nd</sup> sheet); Stage 4 - Sill climbing through the exploitation of faults developed  
1027 during Stage 2; Stage 5 – Sill flattening (not observed at Trachyte Mesa) and late stage  
1028 cooling and relaxation of the intrusion. (b) Schematic illustration highlighting the impact of  
1029 out-of-sequence stacking (equivalent to Stage 2 in (a) on margin geometry and deformation  
1030 structures (as observed in TMTE study area; Fig. 8).

1031

1032 **Fig. 13.** Faulting accompanying sill emplacement. (a) Schematic diagram showing the  
1033 development of a saucer-shaped sill (after Galland et al., 2009). (b) Development of dip slip

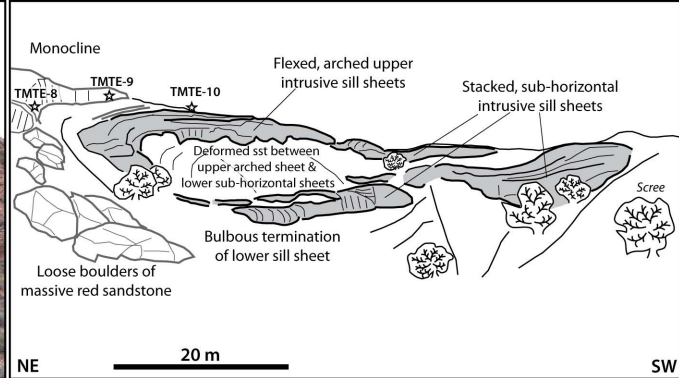
1034 faults at sill tips during two-stage growth model and implications for sill climbing and  
1035 vertical propagation.



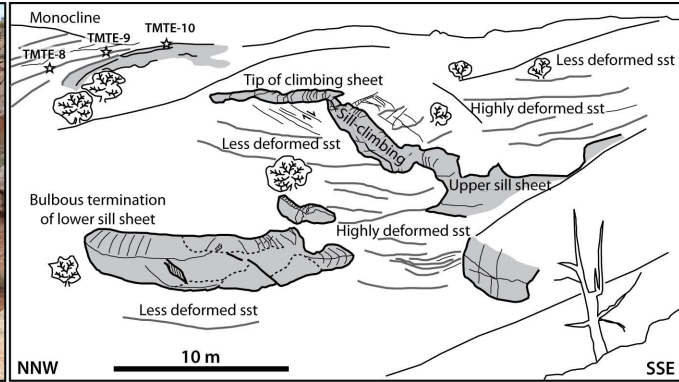


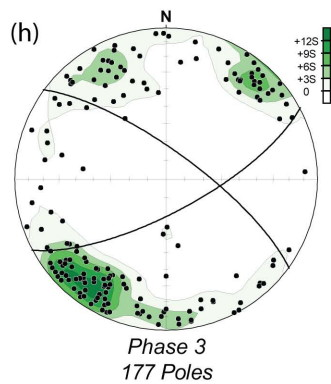
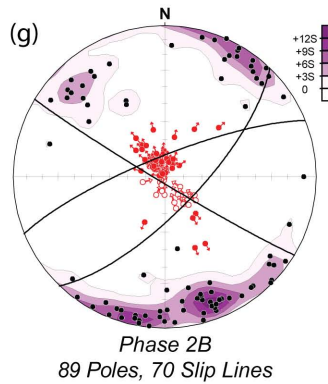
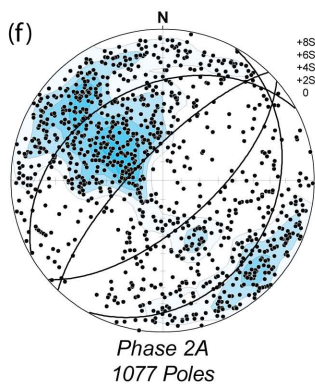
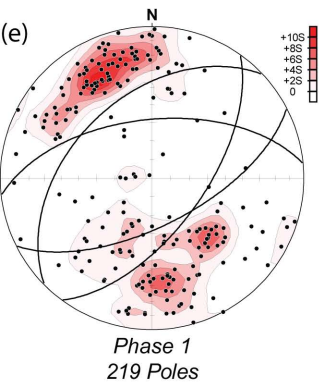
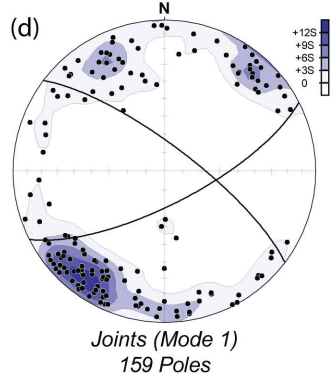
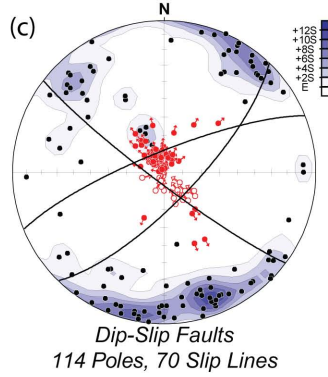
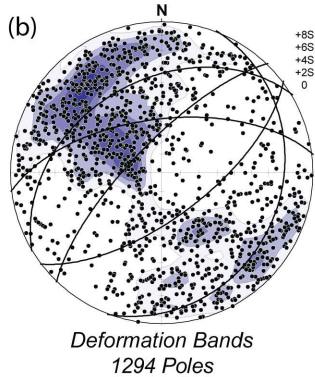
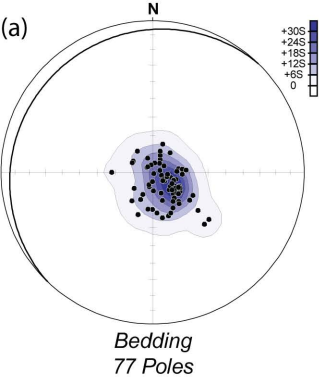


(a)

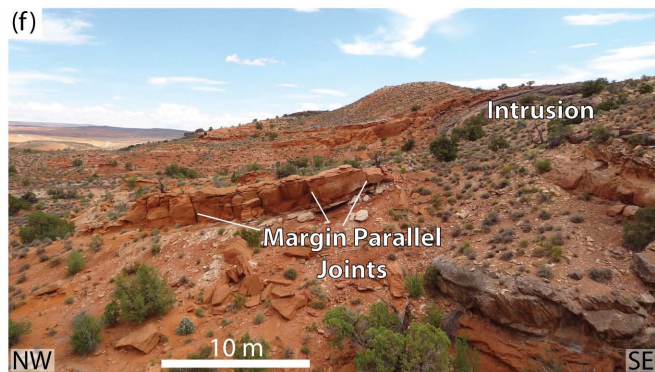
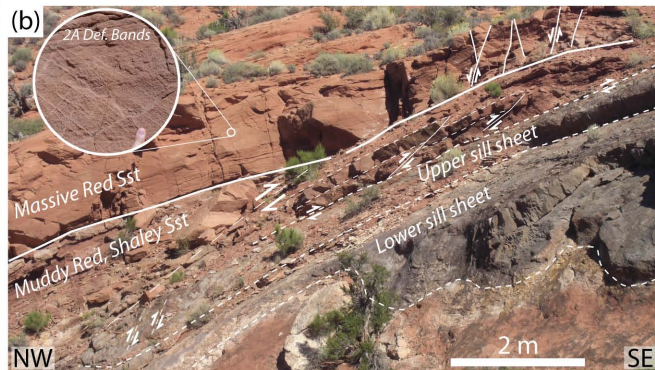
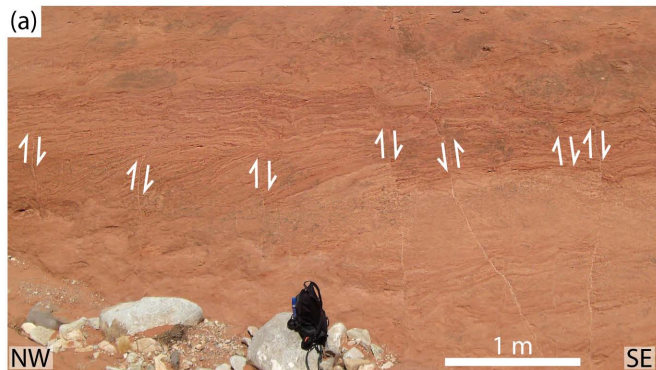


(b)

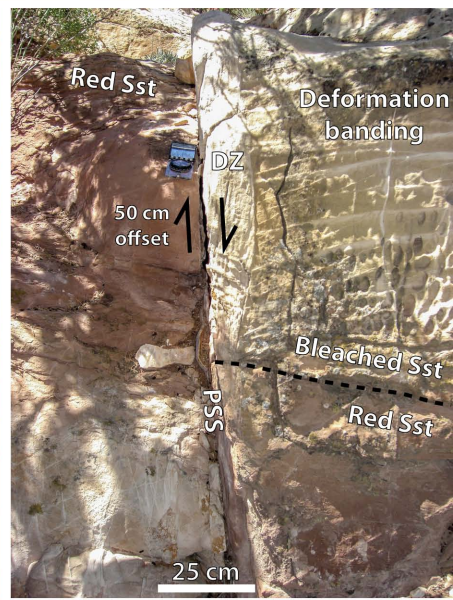
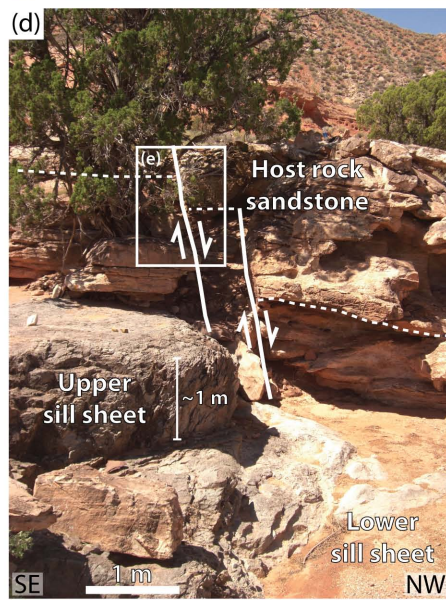
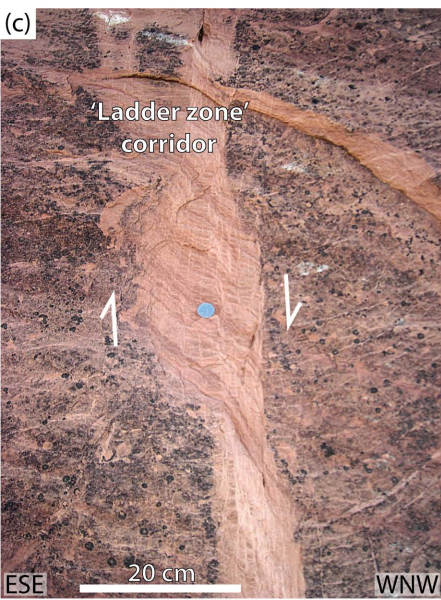
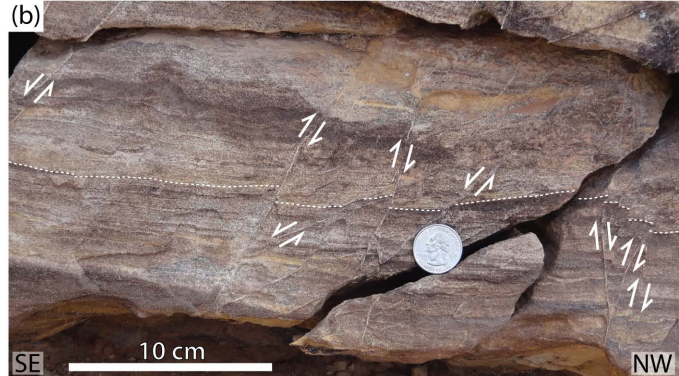
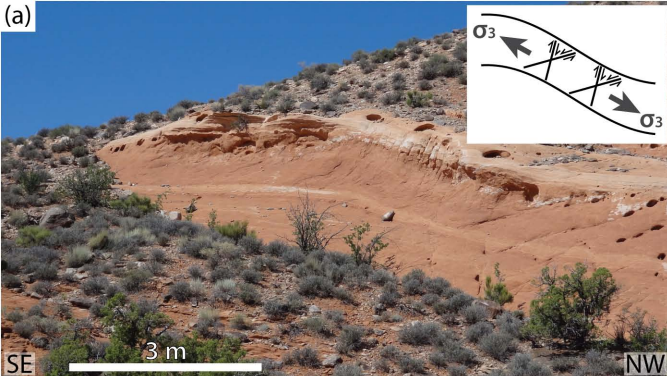


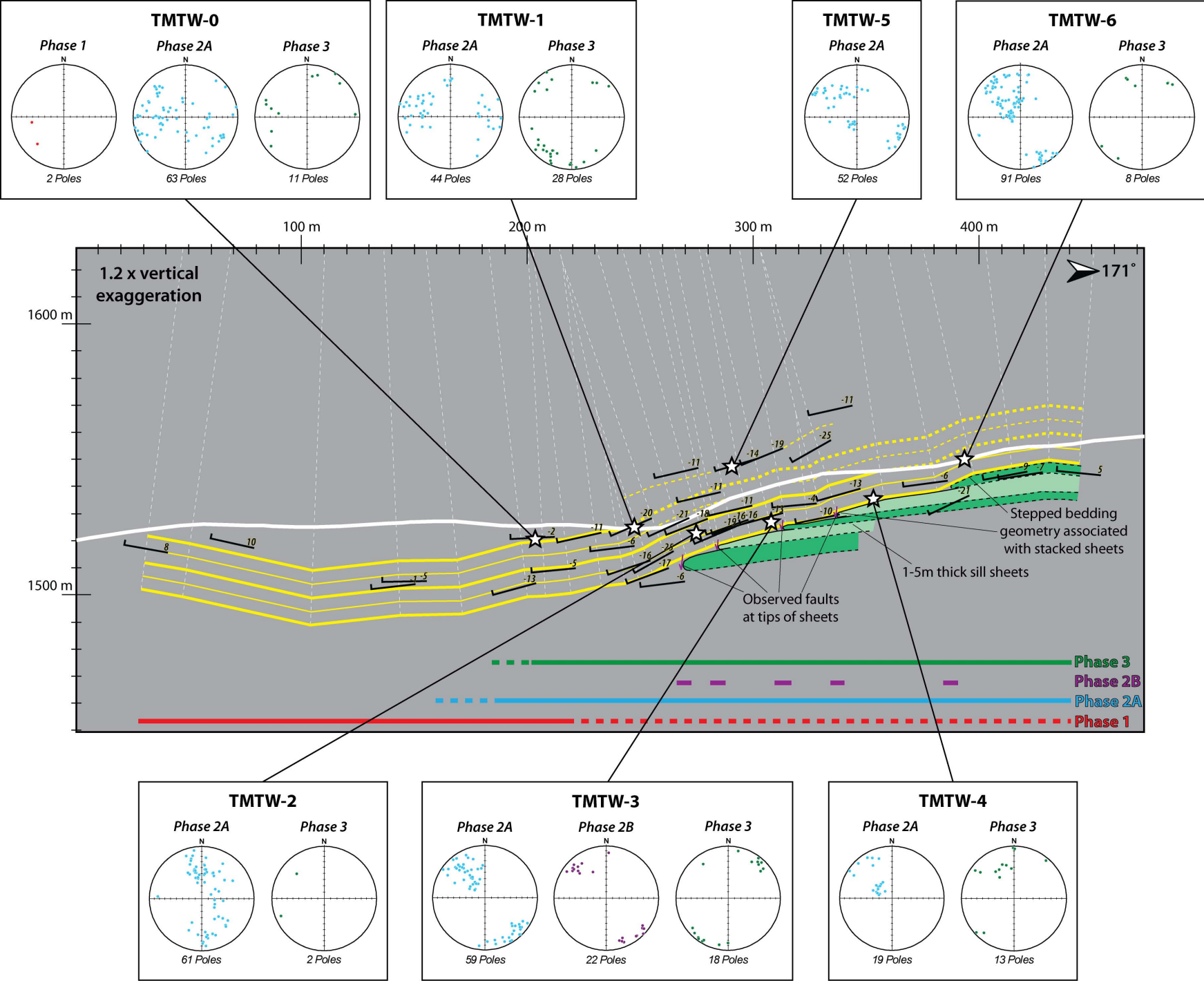






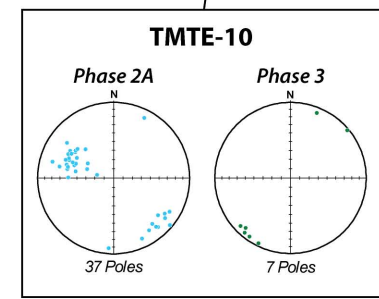
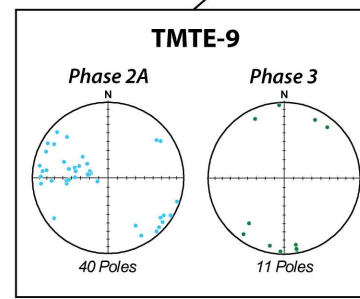
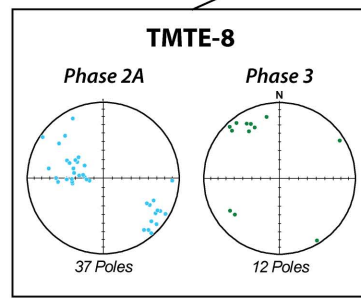
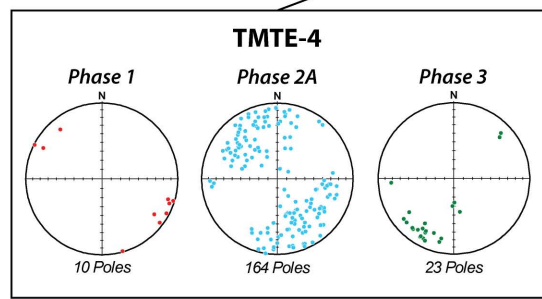
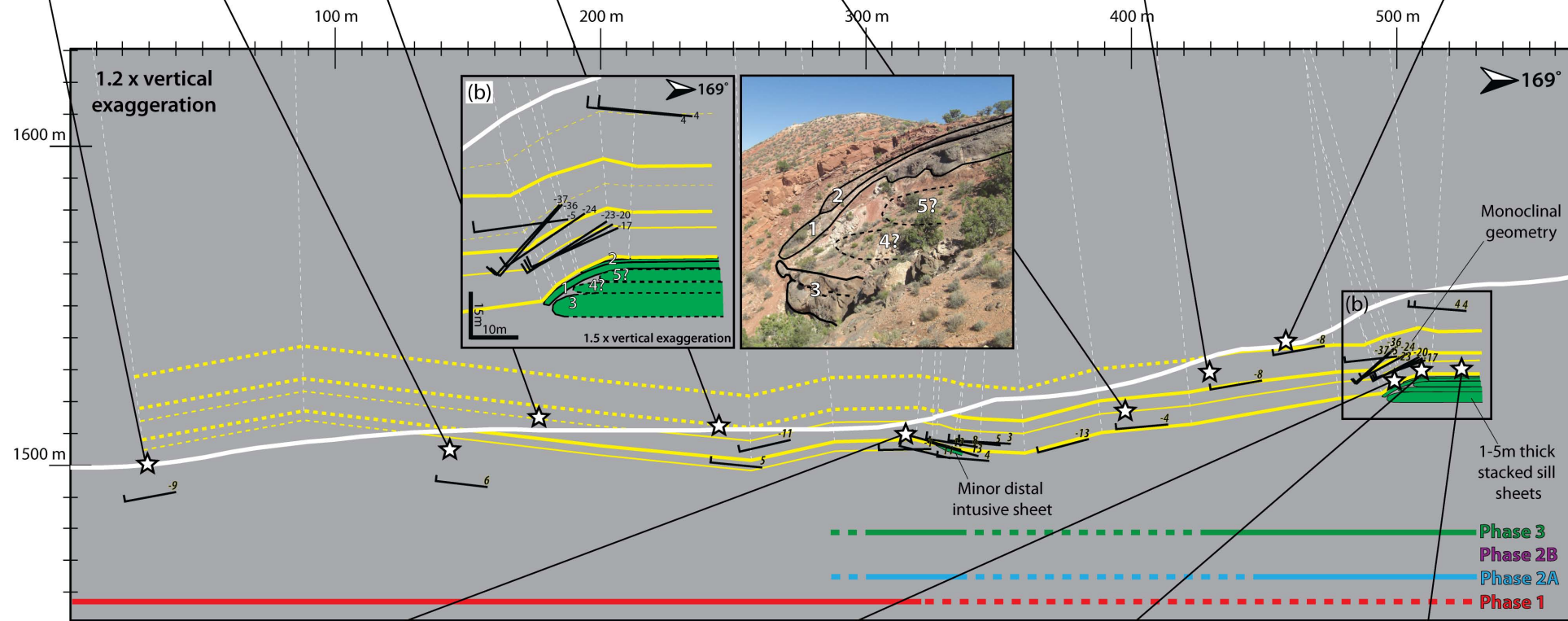
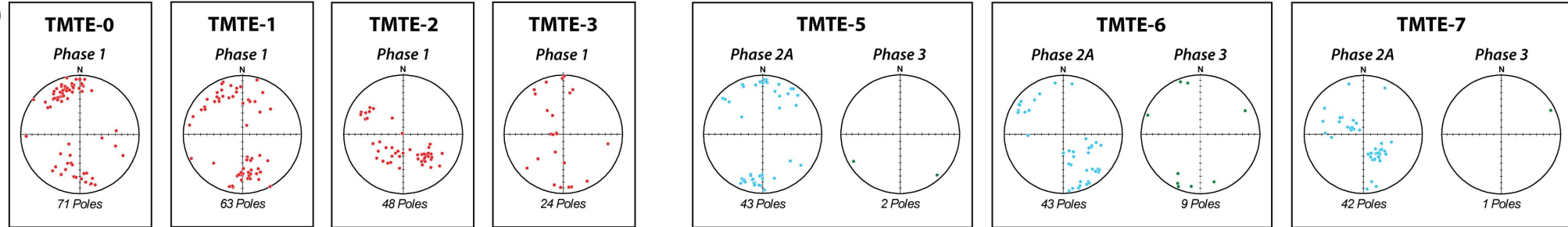


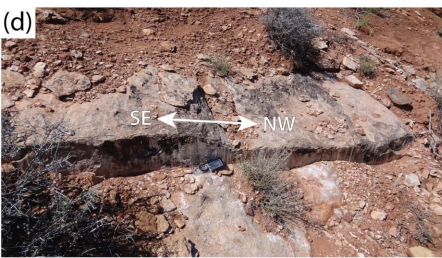
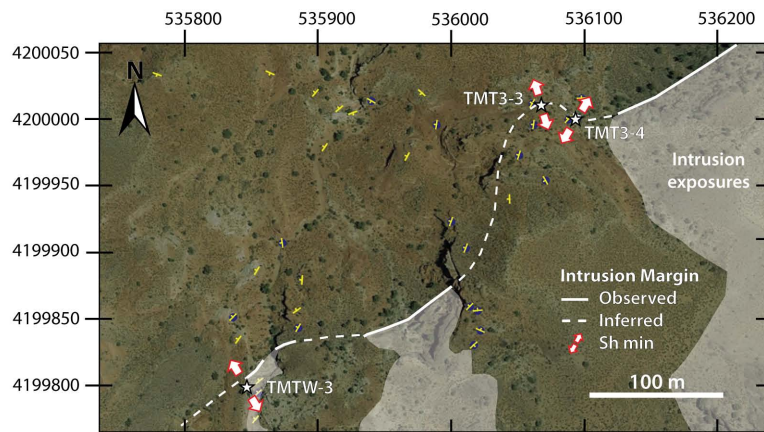
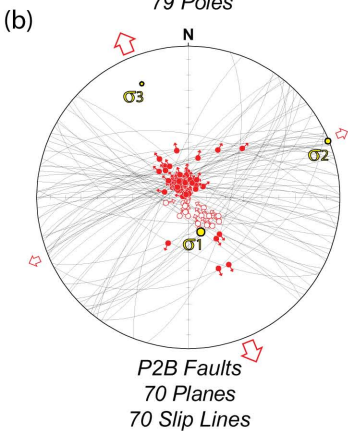
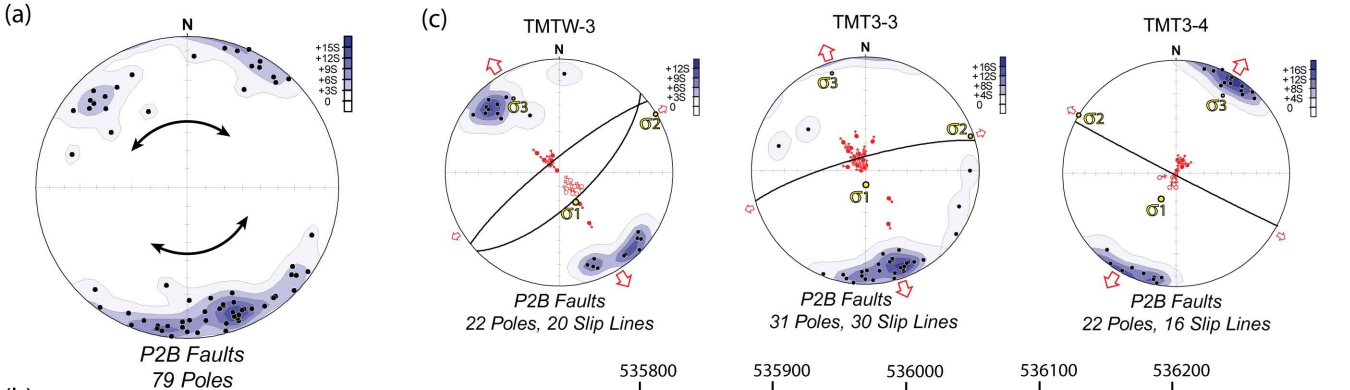




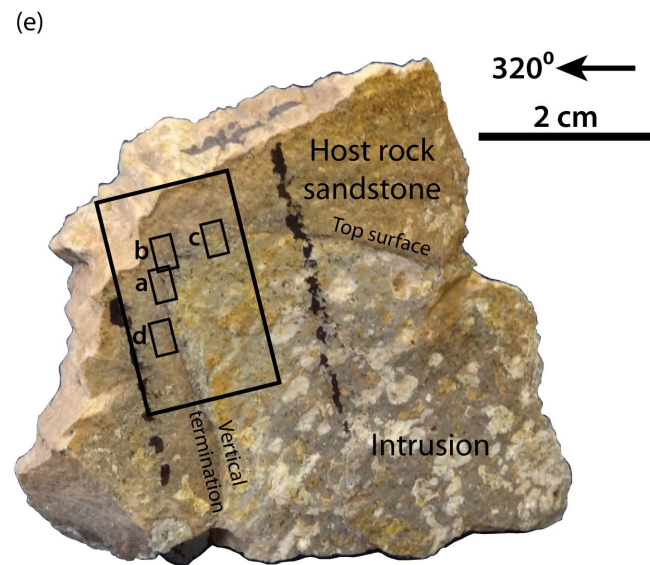
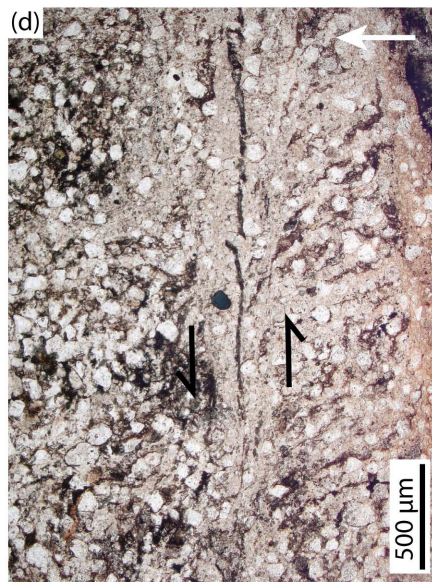
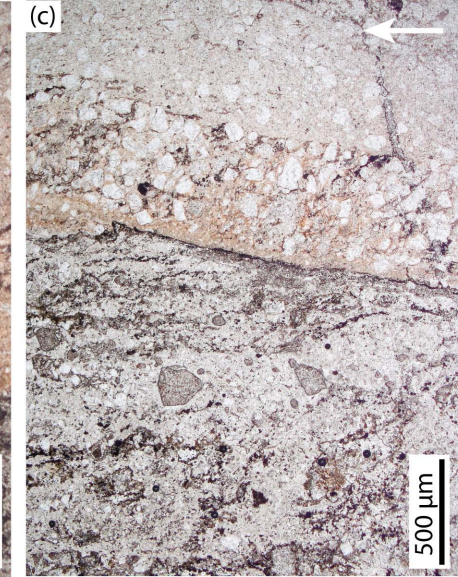


(a)

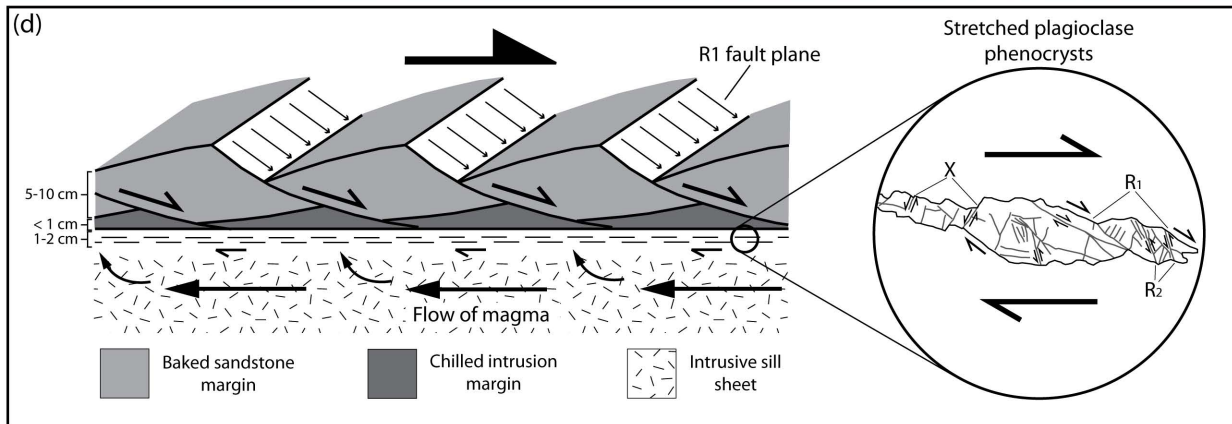
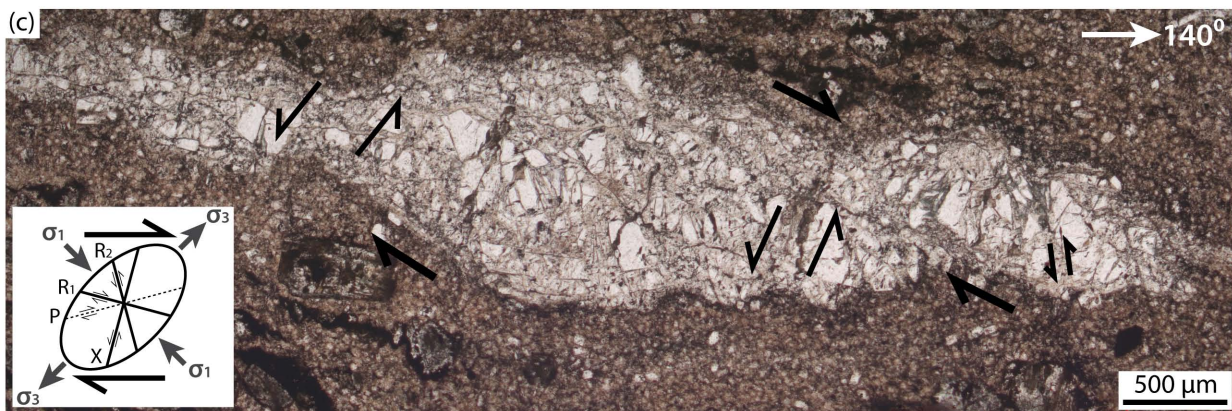
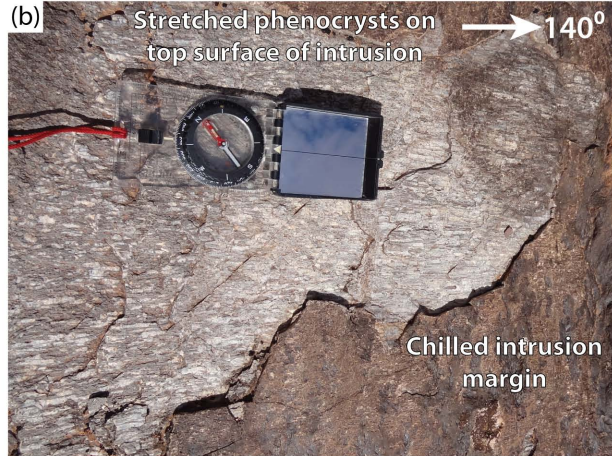
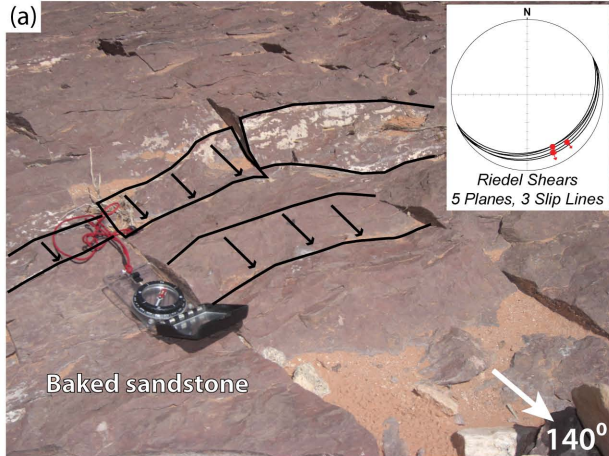


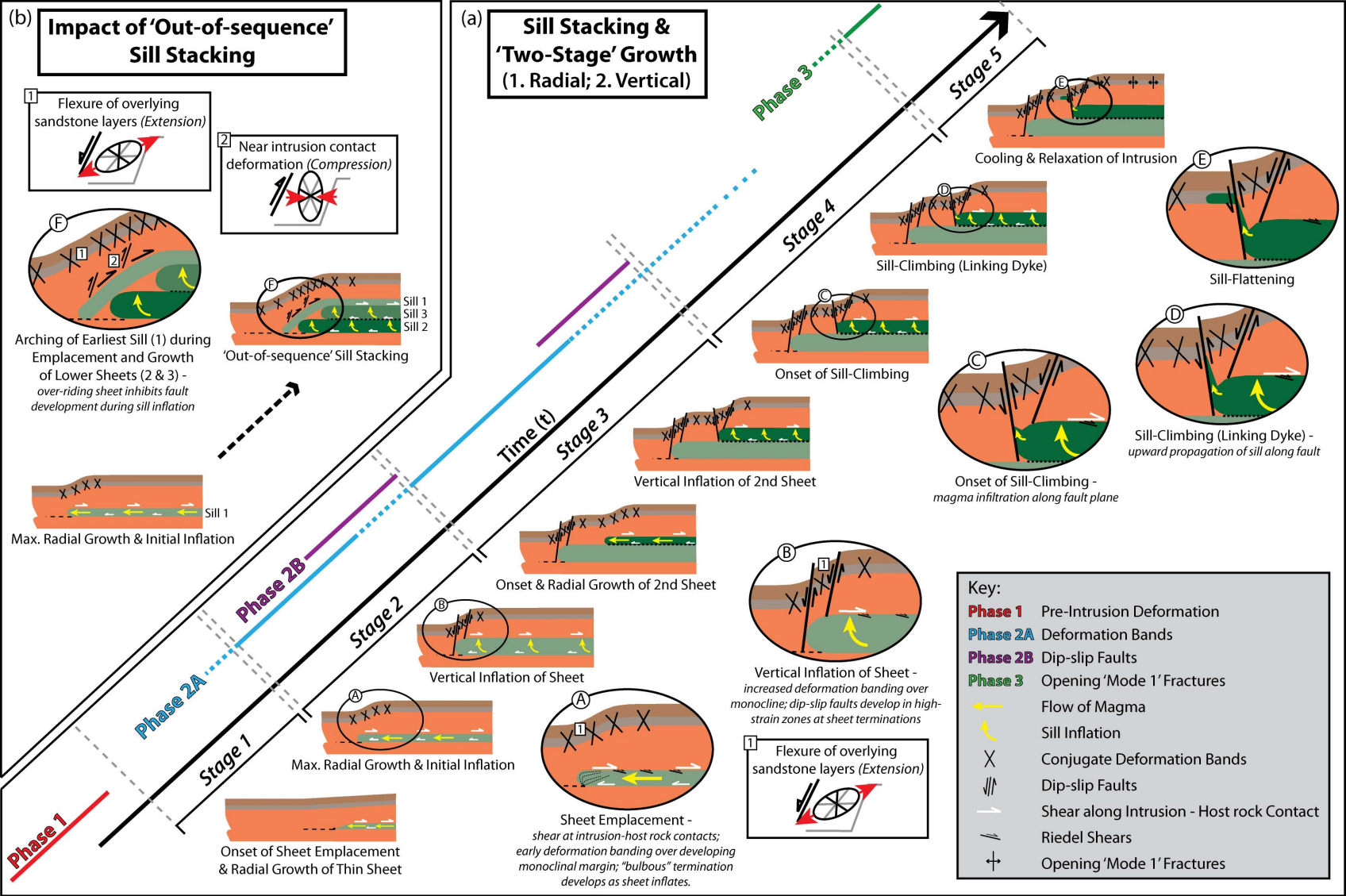










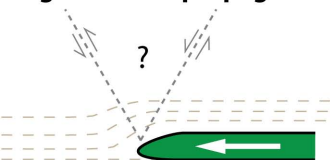


(a)



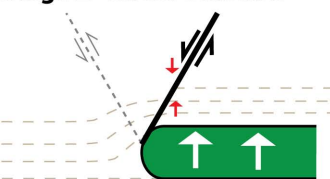
(b)

### Stage 1 - Sheet propagation/ emplacement



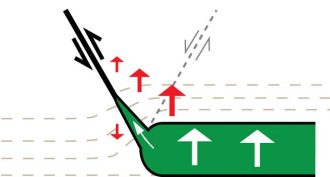
*Initial emplacement of thin sill sheet.  
Bedding moderately deformed by flexure  
and distributed deformation.  
No faults developed.*

### Stage 2 - Sheet Inflation



*Deformation localised at sill tip.  
Normal fault develops.  
No Sill climbing (propagation of magma  
inhibited along fault due to vertical  
compressive stress associated with uplift  
of underlying HW block).*

**or**



*Deformation localised at sill tip.  
Reverse fault develops.  
Sill climbing (magma propagates  
along fault, exploiting void space created  
by uplift of HW block).*